EXPERIMENTAL INVESTIGATION OF HEAT AND FLUID FLOW IN AN ACTUATED IMPINGING JET FLOW

A Thesis Submitted to
the Graduate School of Engineering and Sciences of
Izmir Institute of Technology
in Partial Fulfillment of the Requirements for the Degree of

MASTER OF SCIENCE

in Mechanical Engineering

by
Necati BİLGİN

December 2009
İZMİR

We approve the thesis of **Necati BİLGİN**

Assist. Prof. Dr. Ünver ÖZKOL
Supervisor

Assoc. Prof. Dr. Moghtada MOBEDİ
Committee Member

Assist. Prof. Dr. Şebnem ELÇİ
Committee Member

17 December 2009

Prof. Dr. Metin TANOĞLU
Head of the Department of
Mechanical Engineering

Assoc. Prof. Dr. Talat YALÇIN
Dean of the Graduate School of
Engineering and Sciences

ACKNOWLEDGMENTS

I wish to thank all my committee members, and various faculty members who have encouraged and helped me.

I would like to express my sincere gratitude to my supervisor Assist. Prof. Dr. Ünver ÖZKOL for giving me the opportunity to work under him and for his valuable advises and guidance through the thesis.

I also wishes to express thanks to my labmates, Gürcan DURMAZ, H. İbrahim YANIKTAŞ, and Orçun KOR for their help during my studies.

My parents, Güler and Bülent, and my brother Coşkun have always encouraged and supported my decisions.

Special thanks goes to my darling Zeynep for her support thereby accepting my proposal of marriage.

ABSTRACT

EXPERIMENTAL INVESTIGATION OF HEAT AND FLUID FLOW IN AN ACTUATED IMPINGING JET FLOW

The objective of this work is to how the surface heat transfer and flow characteristics can be affected by jet flow by excitation of which changes the turbulence characteristics of the flow. Main body of this work is experimental analysis; nevertheless some simple numerical analysis is also presented in order to make some comparisons. The hot-wire measurements and flow visualizations are performed. As a flow actuator a loudspeaker is used once the piezo-electric benders were found to be unsuccessful. Acoustic (pressure) wave generated by the loudspeaker travels along the flow system and reaches the jet nozzle where it generates an oscillating component on the mean nozzle velocity. Parameters used on this study are shortly Re=10000, dimensionless jet to plate distance is equal to 6, as a non-dimensional excitation frequency Strouhal number is changed in the range of $0<St<1$, and as for the excitation amplitude, voltages sent to the 20X amplifier are 0.5V, 1.0V and 1.5V.

ÖZET

UYARILMIŞ JET ÇARPMA AKIŞINDAKİ ISI VE AKIŞKAN HAREKETİNİN DENEYSEL ARAŞTIRMASI

Bu çalışmanın amacı, jet akışın uyarılması sonucu yüzeydeki ısı transferinin ve akış karakteristiğinin nasıl etkilendiğinin deneysel olarak incelenmesidir. Bazı basit sayısal analizler yapılarak deneysel sonuçlarla karşılaştırılmıştır. Uyarılmış ve bilinen jet akış için sıcak tel anemometresi ölçümleri ve akış görüntüleme deneyleri yapılmıştır. Akış uyarıcısı olarak hoparlörün ürettiği akustik dalgalar kullanılmıştır. Bunun yanın da piezo malzemeden yapılmış titreştiriciler de kullanılmış fakat bu çalışma için çok uygun bulunmamışlardır. Akustik dalgalar tüm akış sisteminden geçerek jet lülesinin çıkışında akışı uyarmaktadır. Jet parametreleri olarak; Reynolds sayısı 10000, jetin çarpma yüzeyine olan uzaklığının jet çapına oranı 6, birimsiz uyarma frekansı olan Strouhal sayısı için 0 ile 1 ve uyarma genliği olarak da 20X yükselticiye gönderilen voltaj değerleri 0.5, 1, ve 1.5 Volt kullanılmıştır. Yapılan deneyler ve analizler soncunda, jet genişliğinin en çok Strouhal sayısı 0.5 için arttığı gözlemlenmiştir. Yüzeydeki ısı transferi ile ilgili olarak da şu bilgiler elde edilmiştir. Jet akış uyarıldığında, durağan bölgesindeki ısı transfer katsayısı normal jete göre azalmaktadır. Fakat radyal yönde etkinliği artmaktadır. Durağan bölgedeki en büyük ısı transfer düşüşü en fazla jet genişliğinin görüldüğü Strouhal 0.5 ile uyarılmada kaydedilmiştir.

TABLE OF CONTENTS

LIST OF FIGURES

Figure **Page**

LIST OF SYMBOLS

A	Amplitude of loudspeaker
A	Area of heat surface
b_u	Jet width
D	Diameter of the jet
f	Frequency of loudspeaker
h	Heat transfer cooeficient $(Qnet/(\Delta T*A)$
k	Turbulence kinetic energy
k	Conductivity
l	Prandtl's mixing length
Nu	Nusselt number $(h*D/k_{air})$
p	Pressure
Pr	Prandtl number
Q	heat
Re	Reynold number $(Uinlet*D/v)$
St	Strouhal number $(f*D/U_{inlet})$
t	Time
T	Temperature
U	Velocity
u^1	Fluctuation axis velocity
$\bar{u}$	Mean axis velocity
v^1	Fluctuation radial velocity
$\bar{v}$	Mean radial velocity
x	Radial direction coordinate
X	Radial distance of the jet
z	Axis direction coordinate
Z	Nozzle to plate distance

Greek symbols

α	Diffusivity
Δ	Difference
ε	Heat dissipation
μ	Dynamic viscosity
ν	Kinematic viscosity
ρ	Density
τ	Shear stress
ω	Specific heat dissipation

Subscript

Avg	Average
c	Center
f	Fluid
max	Maximum
min	Minimum
T	Turbulence
w	Wall
x	Radyal direction
z	Axis direction

CHAPTER 1

INTRODUCTION

The jet is to impinge the fluid normally on a surface to achieve enhanced coefficients of convective heating, cooling, drying or mass transfer. The jet impingement is widely used in industrial applications such as annealing of metals, cooling of gas turbine blade, cooling in grinding process, tempering of glass plate, drying of textile and paper products. Jet impingement cooling is especially suitable application for high-powered electronic thermal management solutions

Jet impingement cooling technique uses fluid more effective and offers high heat transfer rates. For example, compared with conventional forced convection cooling by confined flow parallel to the cooled surface, impingement produces approximately three times higher heat transfer coefficient at a given flow speed, because the impingement boundary layer are much thinner than that of conventional parallel flow forced convection as shown in Figure 1.1. Given a required heat transfer coefficient, the flow required from an impinging jet may be two orders of magnitude smaller than that required for a cooling using a free wall-parallel flow. The impingement cooling approach offers a compact hardware arrangement with no addition moving parts.

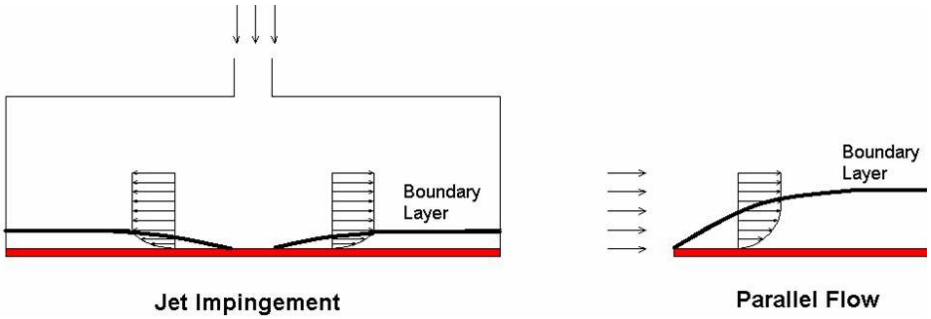

Figure 1.1. Comparison between boundary layer of jet impingement and parallel flow

1.1. Types of Jet Impingement

Impinging jets can be mainly categorized into two groups as gas jets and liquid jets by type of working coolant. Also it can be classified by flow situation and contact between surface and fluid. The fluid may contact with surface in a number of different ways as an application of jet impingement. The most common of these impingement types include free surface, plunging, submerged, confined and wall. A schematic different impingement types are presented in Figure 1.2. A combination of confined and a submerged type jet is used for this study. These kinds of jets are usually found to be suitable for a compact and efficient electronic cooling applications of which this thesis are stemmed from.

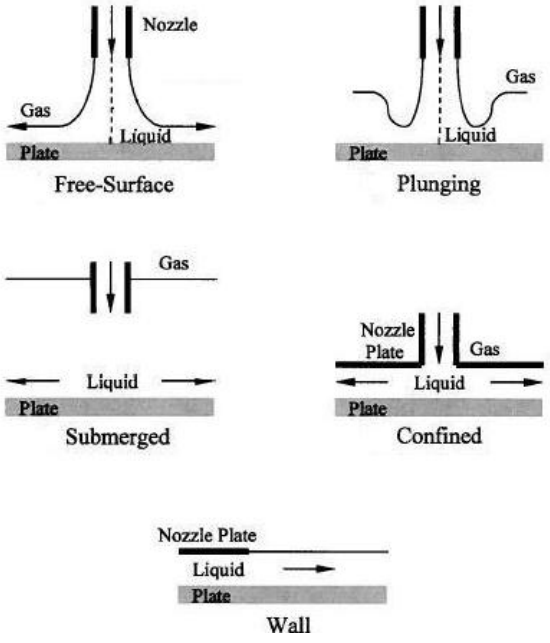

Figure 1.2. Different types of jet impingement
(Source: Wolf, et al.1993)

Jet behavior is correlated by Reynolds number where characteristic length scale is the jet nozzle diameter. Zuckerman and Lior (2005) show that the flow field exhibits laminar flow properties at Re<1000, the flow displays turbulent features at Re>3000 and a transition region occurs between these two regimes.

The jet is sometimes classified and called as round jet or slot jet in according to its nozzle shape also number of jet nozzle is determinative in categorization of the jets, such as single jet and multi jet.

Another type of jet is the synthetic jet. A synthetic jet flow is created by pulsating jet with zero net mass flux. Normally, producing a jet requires an external source of fluid, such as piped-in compressed air or plumbing for water. Synthetic jet flow can be developed in a number of ways, such as with an electromagnetic driver, a piezoelectric driver, or a mechanical driver such as a piston. Each moves a membrane or diaphragm up and down hundreds of times per second, sucking the surrounding fluid into a chamber and then expelling it. Although the mechanism is fairly simple, extremely fast cycling requires high-level of engineering to produce a device that will last in an industrial application.

1.2. Hydrodynamics of Jet Impingement

Major factors of the hydrodynamics of jet flow are the initial flow state, the type of the stationary ambient fluid and the location of the impinging plate from the nozzle. The impingement jet flow where impinging occurs orthogonally on a plane surface is commonly divided into four zones (Figure 1.4).

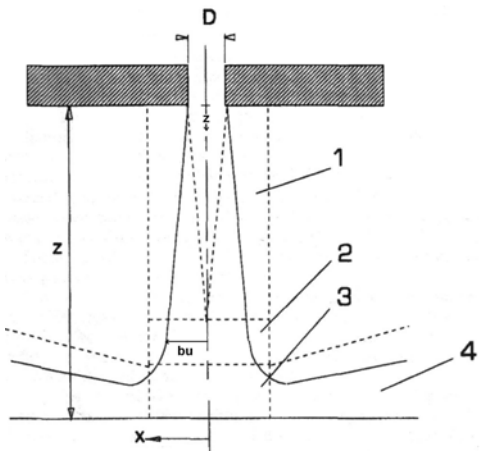

Figure 1.3. Flow zones in an impinging jet. Zone 1, initial mixing region; zone 2, established jet; zone 3, deflection zone; zone 4, wall jet. (Source: Jambunathan, et al. 1992)

(1) There is a developing flow zone where fluid from the surroundings is entrained into the jet, thus reducing the jet velocity. Characteristic of this region is that there is a mixing region where the shear is high surrounding a core region where the fluid velocity (U_c) is almost equal to the nozzle exit velocity (U_{inlet}). The core region is often referred as the potential core even though the flow is not inviscid. A common definition of the end of the core region is the point where $U_c=0.95U_{inlet}$. A core length of six nozzle diameters has been suggested by Gautner et al. (1970) and shown by experimentally.

(2) At greater nozzle to plate spacing the axial velocities reduce with increasing distance from the nozzle exit. An analysis by Schlichting (1968) showed that the fall of the centerline velocity and the jet half width will be directly proportional to the axial distance from the end of the potential core.

(3) The region near the impingement plate is often referred to as the deflection zone where there is a rapid decrease in axial velocity and a corresponding rise in static pressure. The measurements of Tani and Komatsu (1966) showed that this zone extends approximately two nozzle diameters from the plate surface.

(4) After the flow impinging to the wall, there occurs a radial flow on the objected surface. This region is called the wall-jet region. Within the wall jet the transverse velocity rises rapidly to a maximum near to the wall and then falls to zero at greater distance from the wall. The wall jet exhibits higher levels of heat transfer than parallel flow. This appears to be due to turbulence generated by the shear between wall jet and the ambient fluid, which is transported to the boundary layer at the heat transfer surface.

1.3. Jet Parameters

The heat transfer of a jet impingement is a function of many parameters: Reynolds number (Re), Prandtl number (Pr), the ratio of axial distance from nozzle exit to impingement plate over jet diameter (Z/D), jet exit velocity profile and its state at given in Figure 1.4.

In addition to these, the effects of nozzle geometry, flow confinement, turbulence, recovery factor, dissipation of jet temperature are shown to be significant on the heat transfer coefficient.

It would be appropriate to give here two of the commonly used parameters in this thesis; i) Jet half width ($b_{u)}$ which is the width of the jet where U = Uc / 2 at any "z" axis and ii) the spread rate which is defined as the jet half width over nozzle to plate spacing (b_u/z).

1.4. Motivation

In literature, heat transfer coefficient for a jet impingement depends on its turbulence intensity and the radial velocity gradient in the stagnation zone. In turn, both quantities depend on the nozzle geometry and the nozzle to surface spacing (Z) as mentioned in jet parameters and hydrodynamics of jet flow. Objective of many jet applications is to increase heat transfer coefficients on the target hot plate by manipulating one or more of the parameters mentioned.

The objective of this work is to shed some light on to how the surface heat transfer can be affected by jet flow by excitation of which changes the turbulence characteristics of the flow. Using vibrated anchored fins as an actuator near the jet nozzle were the first proposed excitation technique as shown in Figure 1.5. Piezo-electric benders were used for this purpose. However, it was found that piezo-electric benders were in appropriate for the water use. There were some work on the using them for an air jet; however, difficult mounting procedures and fragile nature of the benders did not permit us to pursue on this technique further.

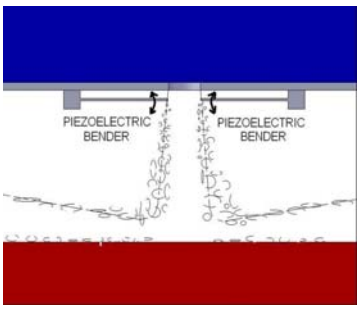

Figure 1.4. Artist view of the action of the piezoelectric benders on the jet turbulence

As an excitation mechanism a loudspeaker is used once the piezo-electric benders were found to be unsuccessful. Acoustic (pressure) wave generated by the loudspeaker travels along the flow system and reaches the jet nozzle where it generates

an oscillating component on the mean nozzle velocity. It is this oscillating component that excites the shear layer of the jet flow. The amplitude and the frequency of the loudspeaker can easily be changed and therefore, its operation is very straightforward.

Overwhelming body of this work is experimental analysis; nevertheless some simple numerical analysis is also presented in order to make some comparisons. Extensive hot-wire measurements and flow visualizations are performed for the experimental body of the work. A commercial code known as FLUENT is used and two different turbulence models available in this code are used for the numerical analysis.

CHAPTER 2

LITERATURE SURVEY

In this chapter, some studies concerning with our objectives in the literature are presented. They consist of non-dimensional parameters, effects of excitation and numerical analysis of turbulent jet flow. Especially, circular confined jet and its excitation are examined.

2.1. Effects of Radial Boundaries and Jet-to-Plate Distance on Jet Flow

The most important geometrical parameters on the jet flow are the radial distance of the side boundaries (X) and the jet-to-plate distance (Z) both affecting the flow at the stagnation region.

Sibulkin (1952) shows that an analytic solution for heat transfer at a stagnation point in a laminar flow shows that Nu is directly proportional to $U_c^{1/2}$ which directly related to the z-distance.

Gardon and Akfirat (1965) investigated the axial variations of velocity and turbulence for jet. Their results showed that the turbulence intensity in a free jet could reach 30 percent at approximately the eight nozzle diameters downstream of the nozzle. The axial distance from the nozzle at which the maximum turbulence intensity occurs appears to coincide with that of the maximum stagnation point heat transfer. Schulunder and Gnielinski (1967) found a similar result that both the maximum turbulence and the maximum stagnation point heat transfer occurring at Z/D=7.5. Gardon and Akfirat (1965) suggested that the increasing level of turbulence causes the heat transfer rate to increase. The increase in the heat transfer rate ceases when the increase in turbulence does not compensate for the fall in the jet velocity. Part of our aim in this study is in the same line with this finding which is to promote the turbulence in jet shear layer to increase the heat transfer.

The radial variation of heat transfer coefficient measured by Gardon and Corbonpue (1962) are given schematically in Figure 2.1. These curves show a local maxima in the heat transfer rate for z/D<6. The heat transfer coefficient for an

impinging circular jet is seen to increase between the stagnation point and x/D=0.5 for small jet-to-plate distances (Z/D<5). A second maximum is produced by a circular jet at approximately x/D=2. Gardon and Carbonpue (1962) also reported that three maximas were visible at radial displacement of 0.5, 1.4, and 2.5 nozzle diameters from the stagnation point for lower Reynolds numbers. The peak at x/D=0.5 has been explained by change in radial velocity where stagnation region ends and the wall-jet region starts. Second maxima at x/D=1.4 can be explained by a transition from laminar to turbulent boundary layer flow. Third maxima occurs at x/D=2 because this location coincides approximately with the point where toroidal vortices, which form in the shear region around the circumference of the jet, strike the plate at Z/D=1.2 and 2 (Popiel and Trass 1982). As the Reynolds number was increased to approximately 20000 the outer maxima merged and only two maxima were seen.

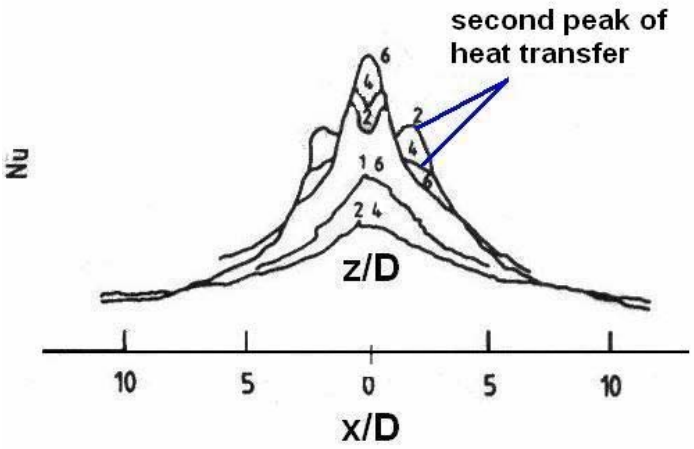

Figure 2.1. Radial variation of heat transfer coefficient
(Source: Gardon and Carbonpue 1962)

There are three reasons for the peaks in the radial distribution of heat transfer; The peak at x/D=0.5 has been explained by the change in the radial velocity, as it accelerates rapidly in the deflection region so does the shear and corresponding heat transfer.

Gardon and Akfirat (1965) suggested that the increase in the heat transfer coefficient with in the range of $1 \leq x/D \leq 2$ can be explained by a transition from laminar to turbulent boundary layer flow. At a greater radial distances from the stagnation point,

a fall in the heat transfer rate occurs because of the reduction in the flow velocity in the radial direction.

Poiel and Trass (1982) reported that the position of the maximum heat transfer at x/D=2 coincides with the point where toroidal vortices, which were originated in the jet shear layer, strike the plate at Z/D=1.2 and 2. They also showed that ring-shaped eddies are formed in the wall jet at the point where the toroidal vortices reach the plate. This coincidence is believed to create increased mixing in this region and therefore increase in heat transfer.

2.2. Effects of Reynolds Number on Jet Flow

Many researchers investigated the effects of Reynolds number on heat transfer coefficient of the jet impingement. Reynolds number (Re) is generally defined as $Re=U_{inlet}*D/\nu$, using initial average flow speed (U_{inlet}), the fluid viscosity (ν), and the characteristic length that is the nozzle exit diameter (D). An isothermal jet's regime is typically categorized by its Reynolds number. The jet flow exhibits laminar flow properties for Re<1000, and the flow shows turbulent characteristics for Re>3000 and transition regions occurs between them. Reynolds number dependence is surely also a function of the turbulence in the incoming flow. Above numbers were given for a mostly turbulent free flow. Martin H. (1977) showed that average Nusselt number of a jet is 19 at Re=2000 (transition to turbulence), Pr=0.7 and Z/D=6 over a circular target of six jet diameter, at Re=100000 the average Nusselt number reaches 212 on the same target. Average Nusselt number of a laminar jet at closer target spacing (Z) at the same Pr and Nu is the range of 2 to 20.

Obtained correlations all give that Nusselt number as a function of Reynolds number. One of these correlations (Jambunathan, et al. 1992) is given in the following

If $Nu \propto \mathrm{Re}^{a}$

$$\text{Where } a = 0.82 - \frac{0.32}{\left[\left(1 + A\left(\frac{x}{D}\right)^{k} + B\left(\frac{x}{D}\right)^{l}\right)\right]\left[\left(1 + C\left(\frac{Z}{D}\right)^{m} + E\left(\frac{Z}{D}\right)^{n}\right)\right]} \qquad (2.1)$$

and A=-1.95, B=2.23, C=0.21, E=0.21, k=1.8, l=2, m=1.25, n=1.5

Nu= f(Re^a,Z/D,x/D) where a= f(x/D,Z/D)

$$Nu / Re^a = K / (1- (x / D)^n \quad (2.2)$$

Where, 1<n<2, a=f(x/D,z/D) and K is constant

This relationship assumes no heat transfer at zero nozzle flow. This assumption is justified by the small temperature differences between the plate and the ambient. The exponent of Reynolds number is also derived which varies only between 0.59 and 0.66 in the range of 0≤x/D≤6.

2.3. Effects of Turbulence Intensity on Jet Flow

Den Ouden and Hoogendoorn (1974) have investigated the effect of small-scale turbulence on heat transfer in impinging jet. They showed that the level of turbulence at the nozzle exit has an impact on the heat transfer at the stagnation point. For example, an increase in the axial turbulence intensity from 0.5 to 3.2 percent (at Re=60000, and Z/D=2) has resulted in an increase in the Nusselt number at the stagnation point from 180 to 215 and has eliminated the local minimum in heat transfer coefficient often seen at small nozzle to plate spacing. However the results of Gardon and Akfirat (1965) showed that the effect of nozzle exit turbulence on heat transfer is relatively small for Z/D>6 where turbulence generated in the shear layer predominates the initial turbulence effects.

2.4. Excited Jets

Researchers first used excited jets to study the structure of the jet and determine the nature of the noise sources. There are two topics in jet excitation; the first topic is the application of jet excitation to influence the large scale coherent structures. The second topic is concerned with the direct implications of excitation on the radiated sound.

Jet excitation occurs when a perturbation alters the instabilities in the shear layer between the jet and the ambient medium. These perturbations may be created naturally or by applied forces. The excitation amplifies the structures of interest and locks them into a regular frequency. The boundary layer between two fluids with different velocities, temperatures, and densities is naturally unstable. As the fluids mix in search of equilibrium, the boundary layer expands forming Kelvin-Helmholtz instability waves.

Hussain and Zaman (1981) noted that "no phase-locked coherent structures could be measured beyond 6 jet diameter downstream of the nozzle exit ($z>6D$). Turbulence intensity in the excited and normal jets is also the same between six and eight jet diameters along the z-direction."

The behavior of the instability waves may be decomposed into modes of oscillation for the convenience of the analysis. Each mode is characterized by an initial growth rate. Additionally, each mode has a preferred frequency or its non-dimensionless form is Strouhal number where maximum amplitude may be obtained. Crow and Champagne (1971) found that the mode with maximum amplitude at the end of the potential core corresponds to the mode with Strouhal number is equal to 0.3. Raman, Zaman and Rice (1989) shows that jet whose initial turbulence intensity varied from 0.15 to 0.5 percent responded to the excitation and also jet response was reduced as core turbulence intensity increased thus more turbulent flows require more powerful actuators to excite them.

Wiltse and Glezer (1992) studied excited air jet by using four piezoelectric actuators placed along the sides of the square jet nozzle exit. They show that at low excitation levels, the flow is not receptive to excitation and induced velocity perturbations are rapidly decreased. Although the amplitude of the actuator displacement is less than one millimeter, the magnitude of the induced velocity perturbation is proportional to the product of the actuator displacement and its frequency. Hence, if the frequency is high enough, the induced velocity perturbation can be quite large and lead to roll up of line vortices. Cross sectional dimension of these vortices are scales with the actuator displacement. Farther downstream from the actuators, the line vortices coalesce and rapidly lose their identity. Nevertheless the formation of these vortices is accompanied by a considerable increase in the cross-stream spreading of the jet shear layer. Hence excitation at frequency with non-uniform amplitude distribution can result in a substantially distorted mean flow.

Wiltse and Glezer (1998) also focus on direct excitation of the small scales within the dissipation range of a free shear flow. They noted that high frequency excitation significantly enhances the turbulent dissipation. Even though the excitation does not alter the mean distribution of the velocity fluctuations within the domain, the dissipation in the forced flow increases relatively to the unforced flow. A small increase in velocity perturbations at high frequencies can lead to significant enhancement of the dissipation and to a decrease in the turbulent kinetic energy within the jet shear layer.

Çelik and Eren (2009) studied about co-axial impinging jets and its flow characteristics. They show that co-axial jet influences a wide area of surface on the target with reference to normal jet. Their study shows that Nusselt number at stagnation point of co-axial jet is higher than the single jet for all Z/D. As the ratio of jet inner diameters to the outer diameter increases, stagnation point Nu increases. There is no significant enhancement of the jet width for co-axial jets. For all values of Z/D, turbulence intensity increases along the axis of the jet (x/D=0) as comparing with a single jet.

2.4.1. Types of Flow Actuators

Flow actuators acts on the flow and create the excitation effect. The actuators may act in different forms; Clifford A. Brown (2005) classified three common excitation types as mechanical, pressure (acoustic) waves, and fluidic actuators (Figure 2.2) and each type's advantage and disadvantage are mentioned at this study.

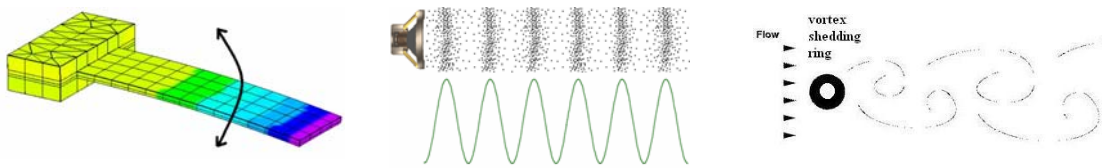

(a) (b) (c)

Figure 2.2. Types of Flow Actuators (a)Piezoelectric (b)Loudspeaker (c)Vortex Shedding Ring

The simplest excitation method is by a mechanical actuator. It is a kind of solid object that is placed in the flow to influence its behaviors. Thus the actuators redirect

the flow and change the amplitudes of the instability waves. Their advantage is that large forces can be applied with them to redirect the flow; however, frequency response is often limited. Common types of the mechanical actuators are vibrating ribbons, thin flap and piezoelectric actuators such as shown in Figure 2.2.a.

Acoustic waves are also used as exciting forces. Commonly this excitation type is generated by a loudspeaker such as in Figure 2.2.b. A Loudspeaker has several advantages for excitations; they are inexpensive and strong and easily controllable in frequency and in amplitude. Although these kinds of properties make them convenient tool, there are limitations on the maximum wave amplitude and frequency compared to mechanical actuators. In addition to this, their size and weight make loudspeakers a poor option for any engineering application that requires mobility. However, they are good choice at the laboratory because generally there is no requirement on the mobility.

The other actuator type is fluidic actuators. This kind of actuators acts on the flow in the form of pulses or vortices. Its main objective is to generate these structures in the flow naturally and utilize their excitation effects. A simple example consists of a vortex shedding ring as shown in Figure 2.2.c, placed nearly upstream of the nozzle exit where the fluids generate exciting vorticies. The frequency of the vortex generation is controlled by the diameter of the ring. Its main difference from the mechanical actuators is to utilize the vortex generation instead of redirection of flow by solid barrier for excitation. Another example of fluidic actuator is a flip-flop actuator. It uses no moving parts; however, the fluid switch paths according to the naturally varying pressure gradient. An another example is a synthetic jet of which pressure varied in a closed container whose one surface consists of a small orifice where fluid is forced in and out periodically, creating the fluidic pulses that excite the jet. New generation of a fluidic actuators type is a spark driven actuators. They excite the flow by a rapid expansion of fluid due to a combustion process or due to temperature expansion. They are limited of frequency response because of the total time required to complete burning process. Its advantages are opportunity of high amplitude and high frequency force for high Reynolds number flows.

2.5. Numerical Analysis of Jet Flow and Turbulence Modeling

Numerical analysis techniques are used for many investigations about jet impingement. Especially turbulence jet flows are preferred rather than laminar jet because in engineering applications and real life jet flow almost appears as turbulent regimes. As a result these investigations focus on turbulence modeling and comparison between their results and experimental data. Thus model errors and judgments of model suitability for jet flow and its heat transfer characteristics are examined. Generally, the studies about k-ε and k-ω turbulence model are argued in this chapter because of contents of our study.

Behnia, Parneix and Durbin (1997) investigate k-ε turbulence models for jet flow as comparing with v^2f turbulence model and experimental data. They focus on turbulence kinetic energy, velocity profiles and Nusselt number on the impinging wall for Z/D=2 and 6 by using turbulence models.

For Z/D=2, they reported that on the stagnation (x/D=0), very little difference in velocity profiles and good agreement between k-ε models and experimental data. At x/D=0.5, the k-ε model predicts low velocities than the experimental results and at x/D=2.5 does not correctly resolve the development of boundary layer in the wall jet region. Behnia et al. (1997) also investigates Nusselt number of jet impingement and they reported that k-ε model significantly over-predicts the local Nusselt number in the stagnation region (170% higher than measured value). For higher values of x/D, the Nusselt number from k-ε model rapidly decreases and approaches the experimental values. In addition to these, k-ε model can not predict the important second peak of Nusselt number occurring near the x/D=2. One of the focus points of Behnia's (1997) investigation is the comparison of turbulence kinetic energy obtained from the k-ε model to experiments. It is found that this model generates a spurious kinetic energy maximum near stagnation region and for this reason can not closely predict heat transfer near stagnation. For Z/D=6, again the turbulent kinetic energy, Nusselt number and velocity profile predictions obtained by the k-ε model were anomalous in magnitude and locations. It over-predicts the stagnation Nusselt number by about 120%.

Also Neil and Zuckerman (2005) indicated that the k-ε model is not recommended for use in the impinging jet problem because of these poor predictions of Nusselt number and physical features.

The k-ω model is also examined by Neil and Zuckerman (2005) also they compared it with k-ε model. In according to their study, the k-ω model produces Nusselt number profiles with a local error of up to 30% compared to experimental Nu values, which is much better than the k-ε model. The k-ω model can generate good predictions of flow properties in the wall jet, both in sublayer and logarithmic region. The k-ω model over-predicts Nu by up to 18% and generated a secondary peak closer to the jet center than found in experiments. The low Re, the k-ω model gives good results by matching the shape of the experimental curves. Their conclusion is the k-ω model is only moderately better than k- ε model; it offers better predictions of Nusselt with a higher computational cost.

Chen and Jaw (1998) studied turbulent free shear flows with turbulent computational models. Their studies show that spread rate of a circular jet is found as 0.123 by using k-ε model. Compared to the experimental results this value should be somewhere between 0.0713 to 0.086. Again, k-ε model largely over predicts.

2.6. Theoretical Approaches of Jet Flow

Prandtl's mixing length theory and Prandtl's second hypothesis are most famous theories used in analysis of shear layer of the jet flow (non-impinging). Some analytical solutions are done by using these theories in the literature. Our results are compared with their solutions at the following chapters. Prandtl's mixing length theory is basically explained that a fluid parcel will conserve its properties for a characteristic length before mixing with the surrounding fluid. Schlichting (1979) describes it as the fluid passes along the wall in turbulent motion, fluid particles coalesce into lumps which move bodily and which cling together for a given traversed length, both in the longitudinal and in the traverse direction, retaining their momentum. Prandtl mixing length theory is used for solving turbulent shear stress caused by momentum transfer due to the velocity fluctuating terms ($\rho\overline{u'v'}$) on the momentum equations (see in Chapter 3) easily. The theory uses following model for the Reynolds Stress;

$$\tau_t = -\rho\overline{u'v'} = \rho l^2 \left|\frac{d\bar{u}}{dy}\right| \frac{d\bar{u}}{dy} \tag{2.3}$$

Where $\upsilon_T = l^2 \left| \frac{d\bar{u}}{dy} \right|$ is usually called as turbulent kinematic viscosity

Prandtl's mixing length theory for shearing stress in turbulent flow is still unsatisfactory in turbulent kinematic viscosity (ν) which vanishes at points where $d\bar{u}/dy$ is equal to zero i.e. at points of velocity maxima. Prandtl assumes that the turbulent kinematic viscosity is proportional to a statistical mean of $\left| d\bar{u}/dy \right|$ in the neighborhood of a velocity maximum. Another assumption was that the dimensions of the lumps of fluid which move in a traverse direction during turbulent mixing are of the same order of magnitude (single length scale) as the width of the mixing zone. After these two assumptions, Prandtl's second hypothesis is obtained as the following equation.

$$\tau_t = \rho x_1 b \left(\overline{u_{\max}} - \overline{u_{\min}} \right) \frac{d\bar{u}}{dy} \tag{2.4}$$

Where x_1 is dimensionless number to be determined experimentally and b is the width of the mixing zone.

These theories make easier to solve the complicated terms of the equations. Analytical solutions of the jet flow problems can be obtained by using them. Tollmein (1931) and Reichardt and Goertler (1941) have solved two dimensional jet flow by using Prandtl's mixing length theory and Prandtl's second hypothesis. Their results will be shown and discussed in Chapter 5.

CHAPTER 3

MODELLING WITH COMPUTATIONAL FLUID MECHANICS

Computerized numerical methods applied to heat and fluid flow is shortly called Computational Fluid Dynamics (CFD). The technique has found application areas in a wide range of industrial and scientific application areas ranging from simple conduction calculations of an electronic card to direct numerical simulations of a turbulent flow. Last 25 to 30 years have been very fruitful for the computer code developers and this is not a exception for the fluid mechanics field. Codes initiated either in academia or in aerospace industry have been commercialized in those years, and continuing doing so. Few examples of these codes are FLUENT (now a part of ANSYS corp. and the code used in this study), Star CFD, ICEPAK, CFDesign.

Application of a CFD code in general consists of several steps. Firstly, the computational domain, the geometry, is defined then it is divided into sub-division that is called “mesh”. Physical and chemical properties that are required are selected and also fluid properties are defined. Appropriate boundary conditions at cells are applied. All these steps are called the pre-processor steps. Following this steps, code solver integrates the governing equations of fluid flow over the domain defined. There are three numerical solution techniques: finite difference, finite element and spectral methods. The finite volume method is developed as a special finite difference formulation. The main differences between these methods are the flow variables are approximated and the discritisation processes. Three mathematical concepts are useful in determining the success of algorithm: convergence, consistency and stability. A finite volume technique has been employed for this study.

The parameters of the problem such as velocity, temperature, pressure are defined at nodes inside each cell. The accuracy is partly governed by the number of cells. On the other hand this costs in terms of computer hardware and calculation time. Therefore it is important to use optimal number of meshes for the domain.

3.1. Governing Equations

3.1.1. Governing Equations with Steady Laminar Flow

The governing equations for the problem are continuity, momentum and energy equations. The fluid that we have used in this study is water and it is a Newtonian fluid. Its thermal properties are taken as constant since the temperature differences expected in the study are small. For the convenience, equations discussed below are given in tensor notation where x, y, z. Cartesian coordinates are denoted as x1, x2, x3 and the x, y, z components of velocity as u1, u2, u3.

Neglecting the body forces the general form of the continuity, momentum, and energy equations can be written in Cartesian tensor form as follows:

Continuity Equation:

$$\frac{\partial}{\partial x_i}(\rho u_i) = 0 \tag{3.1}$$

Momentum Equation:

$$\frac{\partial}{\partial t}(\rho u_i) + \frac{\partial}{\partial x_j}(\rho u_i u_j) = -\frac{\partial p}{\partial x_i} + \frac{\partial}{\partial x_j}\left[\mu\left(\frac{\partial u_i}{\partial x_j} + \frac{\partial u_j}{\partial x_i} - \frac{2}{3}\delta_{ij}\frac{\partial u_i}{\partial x_j}\right)\right] \tag{3.2}$$

The momentum equation written in the above form is known as the Navier-Stokes equation. They are valid for any viscous and compressible Newtonian fluid.

For an incompressible fluid flow equation can be simplified further as:

$$\frac{\partial u_i}{\partial x_i} = 0 \qquad \text{where } i = 1, 2, 3 \tag{3.3}$$

which can be written in Cartesian coordinates for 2-D flow as :

$$\frac{\partial \mathrm{u}}{\partial \mathrm{x}} + \frac{\partial v}{\partial \mathrm{y}} = 0 \tag{3.4}$$

When the density and viscosity are taken as constant and there is no body force in all direction and the fluid is incompressible, the Navier-Stokes equation can be simplified to in as follows:

$$\frac{\partial}{\partial \mathrm{t}}(\mathrm{u_i}) + \frac{\partial}{\partial x_j}(u_i u_j) = -\frac{1}{\rho}\frac{\partial \mathrm{p}}{\partial \mathrm{x_i}} + \nu \frac{\partial}{\partial \mathrm{x_j}}\left[\left(\frac{\partial \mathrm{u_i}}{\partial \mathrm{x_j}}\right)\right] \tag{3.5}$$

Which can be rewritten in x and y components for 2-D flow as:

x-momentum:

$$\frac{\partial u}{\partial \mathrm{t}} + \mathrm{u}\frac{\partial u}{\partial x} + \mathrm{v}\frac{\partial u}{\partial y} = -\frac{1}{\rho}\frac{\partial \mathrm{p}}{\partial \mathrm{x}} + \nu\left[\frac{\partial^2 u}{\partial x^2} + \frac{\partial^2 u}{\partial y^2}\right] \tag{3.6}$$

y-momentum:

$$\frac{\partial v}{\partial \mathrm{t}} + \mathrm{u}\frac{\partial v}{\partial x} + \mathrm{v}\frac{\partial v}{\partial y} = -\frac{1}{\rho}\frac{\partial \mathrm{p}}{\partial \mathrm{y}} + \nu\left[\frac{\partial^2 v}{\partial x^2} + \frac{\partial^2 v}{\partial y^2}\right] \tag{3.7}$$

Energy equation in terms of fluid enthalpy is defined by:

$$\rho\frac{D\mathrm{h}}{D\mathrm{t}} = \nabla(k\nabla T) + \frac{D\mathrm{p}}{D\mathrm{t}} + \Phi + q \tag{3.8}$$

Where $h = U + \frac{\mathrm{p}}{\rho}$ is fluid enthalpy.

The left hand side of the equation 3.8 is called the convective term. The first term in the right hand side is the rate of heat diffusion (conduction) in the fluid. The second term is the rate of reversible work done on the fluid by compression. The third term is the rate of viscous dissipation per unit volume and finally the last term

represents the heat generation per unit volume. Internal energy of the fluid is given as du= Cv.dT, where Cv is the specific heat at constant volume.

For an incompressible fluid with constant thermal conductivity, no viscous heat dissipation, no compression work and without heat generation inside, the energy equation reduces to

$$\frac{\partial \mathrm{T}}{\partial \mathrm{t}} + u\frac{\partial \mathrm{T}}{\partial \mathrm{x}} + \mathrm{v}\frac{\partial \mathrm{T}}{\partial \mathrm{y}} = \alpha\left(\frac{\partial^2 \mathrm{T}}{\partial \mathrm{x}^2} + \frac{\partial^2 \mathrm{T}}{\partial \mathrm{y}^2}\right) \qquad \text{where } \alpha = \frac{\mathrm{k}}{\rho Cp} \tag{3.9}$$

3.1.2. Governing Equations with Steady Turbulent Flow

Turbulent flow is characterized by disorderly displacement of individual volumes of fluid within the flow. Velocity, temperature, pressure and other properties change continuously in time at every point of a turbulent flow. The governing equations describing the conservation of mass, momentum, and energy are valid for turbulent as well as for laminar flows. However those given quantities are called instantaneous values for a turbulent flow since particularly the velocity and temperature are known to fluctuate turbulently. In turbulent flows, the instantaneous values always vary with time, and the variations have irregular fluctuations about mean values. These fluctuations are significant and can not by no means neglected. These instantaneous parameters can be broken into time averaged (mean) and fluctuating parts as follows and this is called Reynolds decomposition:

$$\begin{aligned} u &= \bar{u} + u' & p &= \bar{p} + p' \\ v &= \bar{v} + v' & T &= \bar{T} + T' \\ w &= \bar{w} + w' & \rho &= \bar{\rho} + \rho' \end{aligned} \tag{3.10}$$

A time record of an instantaneous velocity component in turbulent flow schematically looks like the one in Figure 3.1 where u' is the fluctuating part and the $\bar{u}$ is the mean component. This time averaged mean is defined as

$$\bar{u} \equiv \frac{1}{\Delta t} \int_{t_0}^{t_0+\Delta t} u dt \tag{3.11}$$

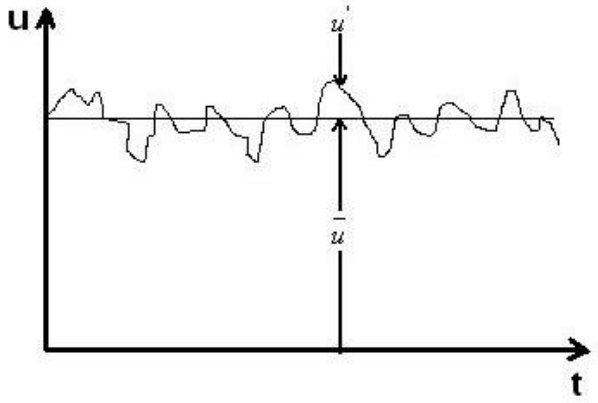

Figure 3.1. A schematic of the variation of the turbulent velocity component u with time

Our computational domain is assumed steady and two-dimensional in the mean sense; therefore, the only x and y components of the velocity are solved.

Continuity Equations:

With the above assumptions, inserting Eqs. (3.10) into Eq. (3.4), (3.6), (3.7), the continuity, the momentum and energy equations are obtained for turbulent flow as follows. Here time averaging applied for the continuity and for the details please refer to any advanced fluid text books such as Convection Heat Transfer (V. Arpacı 1984).

$$\frac{\partial \bar{\mathrm{u}}}{\partial \mathrm{x}} + \frac{\partial \bar{v}}{\partial \mathrm{y}} = 0 \text{ and } \frac{\partial u'}{\partial x} + \frac{\partial v'}{\partial y} = 0 \tag{3.12}$$

Momentum equations:

Substituting the Reynolds decomposed velocity components and pressure into Eq. (3.6) for the momentum equations for turbulent flow and applying time averaging we will get

$$\bar{\mathrm{u}}\frac{\partial \bar{u}}{\partial x} + \bar{\mathrm{v}}\frac{\partial \bar{u}}{\partial y} = -\frac{1}{\rho}\frac{\partial \bar{\mathrm{p}}}{\partial \mathrm{x}} + \frac{1}{\rho}\left[\mu\left(\frac{\partial^2 \bar{u}}{\partial x^2} + \frac{\partial^2 \bar{u}}{\partial y^2}\right) - \frac{\partial}{\partial x}\left(\rho\overline{u'^2}\right) - \frac{\partial}{\partial y}\left(\rho\overline{u'v'}\right)\right] \tag{3.13}$$

$\mu \frac{\partial \bar{u}}{\partial y}$: Viscous shear stress is responsible for the molecular diffusion.

$\rho \overline{u'v'}$: Turbulent shear stress caused by momentum transfer due to the velocity fluctuations.

Energy equation:

The mean turbulent energy equation can also be obtained similarly and it is given as:

$$\bar{u}\frac{\partial \bar{T}}{\partial x} + \bar{v}\frac{\partial \bar{T}}{\partial y} = \frac{1}{\rho c_p}\left[\frac{\partial}{\partial y}\left(k\frac{\partial \bar{T}}{\partial y} - \rho c_p \overline{u'T'}\right)\right] \tag{3.14}$$

In which the last term is responsible from the mean turbulent heat diffusion which speeds up the heat transfer process tremendously by the turbulent mixing. It is the aim of this study to boost up this term to enhance heat transfer.

3.2. Turbulence Modeling

As it is understood from the above formulation, we have more unknowns then the equations to solve due to the extra turbulent terms. This can be handled only if these terms are somehow modeled with the help of known quantities. This is called closure problem. In this study, k-ε and k-ω turbulence models were used for the solution of our axisymmetric problem since they were readily available in the code that we used.

3.2.1. k-ε Turbulence Model

It would be appropriate here to give a very short description of these models and mention their similarities and differences. The standard k-ε model is one of the earliest turbulence models that have been developed and used in the literature. It is known to handle well some simple shear flows but also known to perform very badly in most of

the other cases. Here we used it to see how it is going to perform against our experiments. Its some of the advantages are

- It is a simple turbulence model for which only initial and/or boundary conditions need to be supplied
- Excellent performance for many simple high Reynolds number flows
- Well established; the most widely validated turbulence model

The turbulence kinetic energy (k) is defined as $k = \frac{1}{2}\left(\overline{\left(u_i^{'}\right)^2} + \overline{\left(u_j^{'}\right)^2}\right)$ and the specific momentum dissipation rate (ε) can be obtained from following transport equations. (Wilcox 2006)

Turbulence kinetic energy:

$$\frac{\partial k}{\partial t} + u_j \frac{\partial k}{\partial x_j} = \tau_{ij} \frac{\partial u_i}{\partial x_j} - \varepsilon + \frac{\partial}{\partial x_j}\left[\left(\upsilon + \nu_T / \sigma_k\right)\frac{\partial k}{\partial x_j}\right] \tag{3.15}$$

Dissipation rate:

$$\frac{\partial \varepsilon}{\partial t} + u_j \frac{\partial \varepsilon}{\partial x_j} = C_{\varepsilon 1}\frac{\varepsilon}{k}\tau_{ij}\frac{\partial u_i}{\partial x_j} - C_{\varepsilon 2}\frac{\varepsilon^2}{k} + \frac{\partial}{\partial x_j}\left[\left(\nu + \nu_T / \sigma_\varepsilon\right)\frac{\partial \varepsilon}{\partial x_j}\right] \tag{3.16}$$

Where,

$\nu_T = C_\mu k^2 / \varepsilon$, $C_{\varepsilon 1} = 1.44$, $C_{\varepsilon 2} = 1.92$, $C_\mu = 0.09$, $\sigma_k = 1.0$, $\sigma_\varepsilon = 1.3$

3.2.2. k-ω Turbulence Model

Here again, k stands for the turbulent kinetic energy and the ω is the specific dissipation rate which is defined as (David C. Wilcox, 2006)

Turbulent kinetic energy:

$$\frac{\partial k}{\partial t} + u_j \frac{\partial k}{\partial x_j} = \tau_{ij}\frac{\partial u_i}{\partial x_j} - \beta^* k\omega + \frac{\partial}{\partial x_j}\left[\left(\nu + \sigma^*\frac{k}{\omega}\right)\frac{\partial k}{\partial x_j}\right] \tag{3.17}$$

Specific dissipation rate:

$$\frac{\partial \omega}{\partial t}+u_j\frac{\partial \omega}{\partial x_j}=\alpha\frac{\omega}{k}\tau_{ij}\frac{\partial u_i}{\partial x_j}-\beta\omega^2+\frac{\sigma_d}{\omega}\frac{\partial k}{\partial x_j}\frac{\partial \omega}{\partial x_j}+\frac{\partial}{\partial x_j}\left[\left(\nu+\sigma\frac{k}{\omega}\right)\frac{\partial \omega}{\partial x_j}\right] \quad (3.18)$$

Where,

$$\alpha=\frac{13}{25},\ \beta_0=0.0708,\ \beta^*=\frac{9}{100},\quad \sigma=\frac{1}{2},\ \sigma^*=\frac{3}{5},\ \sigma_{d0}=\frac{1}{8}$$

$$\beta=\beta_0 f_\beta,\quad f_\beta=\frac{1+85X_\omega}{1+100X_\omega},$$

Cross-diffusion terms: $\sigma_d=\begin{cases}0, & \frac{\partial k}{\partial x_j}\frac{\partial \omega}{\partial x_j}\le 0\\ \sigma_{d0}, & \frac{\partial k}{\partial x_j}\frac{\partial \omega}{\partial x_j}>0\end{cases}$

$X_\omega\equiv\left|\frac{\Omega_{ij}\Omega_{jk}S_{ki}}{(\beta^*\omega)^3}\right|$ is zero for two-dimensional flows.

Mean rotation tensor: $\Omega_{ij}=\frac{1}{2}\left(\frac{\partial u_i}{\partial x_j}-\frac{\partial u_j}{\partial x_i}\right)$

Mean strain rate tensor: $S_{ij}=\frac{1}{2}\left(\frac{\partial u_i}{\partial x_j}+\frac{\partial u_j}{\partial x_i}\right)$

3.2.3. V2F Turbulence Model

This model has not been applied in this study; nevertheless, we have made some comparisons with the results obtained with it from literature. Therefore, it would be appropriate here to give a short information on it.

V^2F model is also known as 'normal velocity relaxation model'. This model uses an eddy viscosity to increase stability (rather than using a full Reynolds Stress Model) with two additional differential equations beyond those of the k-ε model. It uses the turbulent stress normal to the stream lines (referred to as V^2) to determine the turbulent eddy viscosity rather than the scalar turbulence intensity used in the k-ε model.

The V^2F model requires a dense wall grid. Despite its moderately high computational cost, it is acknowledged as one of the best predictors of Nu distribution. Also it can predict occurrence, position, and magnitude of the secondary Nu peak for low Z/D so it closely matches experimental results.

3.3. Computational Domain

All analysis was done at steady state condition. Although the disturbed flow must be solved by time dependent equations in order to resolve the effect of the disturbances, steady state Reynolds averaged equations are solved and those are compared with the undisturbed experiments and with the literature.

3.3.1. Discritisation

Computational domain is meshed with Cartesian type meshes, using finer meshes in the shear and boundary layers where velocity gradients are higher. Computations are performed with implicit; pressure based first order upwind differencing scheme of finite volume analysis in a two dimensional axisymmetric domain. Continuity equation is incorporated in the solver as a pressure correction scheme by so called the SIMPLE algorithm.

The finite volume method is a method for representing and evaluating partial differential equations. Values are calculated at discrete places on the meshed geometry. "Finite volume" refers to the small volume surrounding each node point on the mesh. In the finite volume method, volumes integrals contain a divergence term are converted to surface integrals, using the divergence theorem. These terms are then evaluated as fluxes at the surfaces of each finite volume. Because the flux entering a given volume is identical to that leaving the adjacent volume, these methods are conservative (Figure 3.2). An advantage of the finite volume method is that it is easily formulated to allow

for unstructured meshes and therefore can be easily adapted to complex geometries. The method is used in many computational fluid dynamics packages.

The SIMPLE algorithm is an iterative procedure for the calculation of pressure and velocity fields. Starting from an initial pressure field p*, its principle steps are:

1- Solve the discretised momentum equation to yield the intermediate velocity field (u*, v*).

2- Solve the continuity equation in the form of an equation for pressure correction p_l.

3- Correct pressure and velocity

4- Solve all other discretised transport equations for scalars Φ.

5- Repeat until the field p, u, v and Φ have all converged.

3.3.2. Boundary Conditions

All CFD problems are defined in terms of initial and boundary conditions. Boundary conditions specify the flow and the thermal variables on the boundaries of physical model. They are, therefore, a critical component of CFD simulations and it is important that they are specified appropriately. All the boundary conditions that are used in jet domain are showed in Figure 3.2.

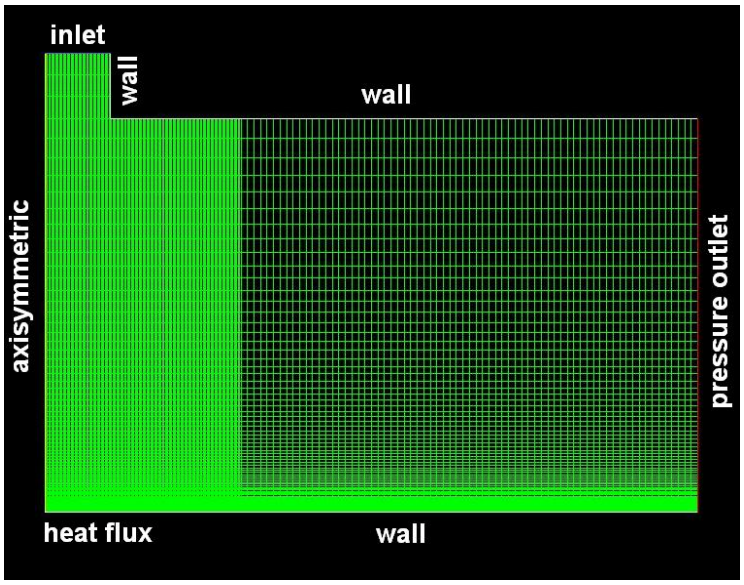

Figure 3.2. Mesh and Boundary Conditions

Inlet boundary conditions:

In our domain, uniform velocity profile is assigned as inlet boundary condition. The flow direction must be through inside of the domain (Figure 3.3). Velocity magnitude for inlet is assigned as 1 m/s for Re=10000. Its mathematical representation is u(1,j)=1 for all j on the edge of the boundary.

Wall and heat flux boundary conditions:

In viscous flow any solid object applies shear stress on the flow through its surfaces which is called no-slip condition. This is defined as u=0, v=0, w=0 for the flow at any rigid wall.

Also thermal properties can be added to the wall as temperature or heat flux. FLUENT uses following equations to determine the wall surface temperature adjacent to a fluid cell as

$$q = h_f \left(T_w - T_f\right) + q_{rad} \qquad T_w = \frac{q - q_{rad}}{h_f} + T_f \tag{3.19}$$

In our computational domain 3 mm thickness aluminum impinging plate is used as a source of heat flux of 50 W/cm^2. Also radiation is neglected.

Pressure outlet boundary conditions:

Pressure outlet boundary conditions require the specification of the static (gauge) pressures at the outlet boundaries.

If N is the total number of nodes in the flow direction, the equations are solved for cells up to I= N-1. Before the relevant equations are solved, the values of the flow variables at the assumed nodes outside the domain are determined by extrapolation from the interior on the assumption of zero gradients at the outlet plane.

The pressure value of outlet boundary condition is taken as 0 Pa. Note that the outlet boundary is positioned far away from jet inlet as it can not affect the main jet flow. 10D distance between inlet and outlet is found appropriate for this.

Axis boundary condition:

The axis boundary type must be used as the centerline of an axisymmetric geometry (Figure 3.3). It can also be used for the centerline of a cylindrical-polar quadrilateral or hexahedral grid. Axis boundaries simply imply that the gradient of the angular coordinate is zero.

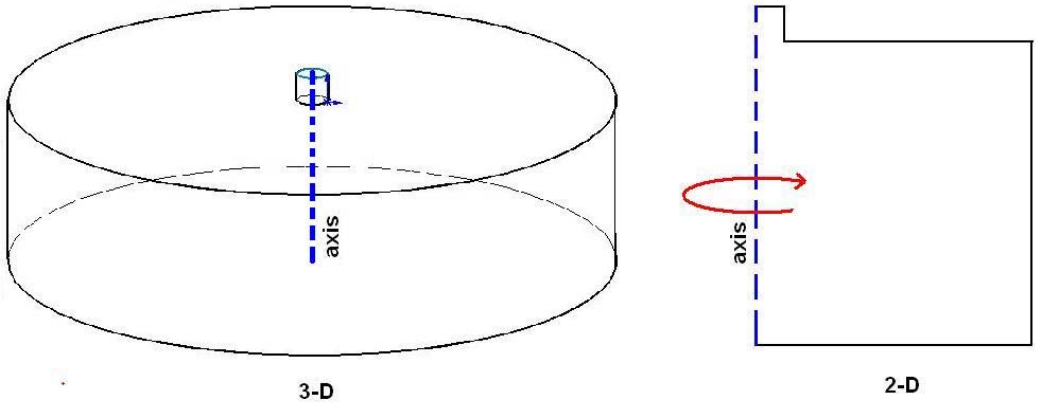

Figure 3.3. Axis-symmetric boundary condition

It generates the meshes as Figure 3.4.

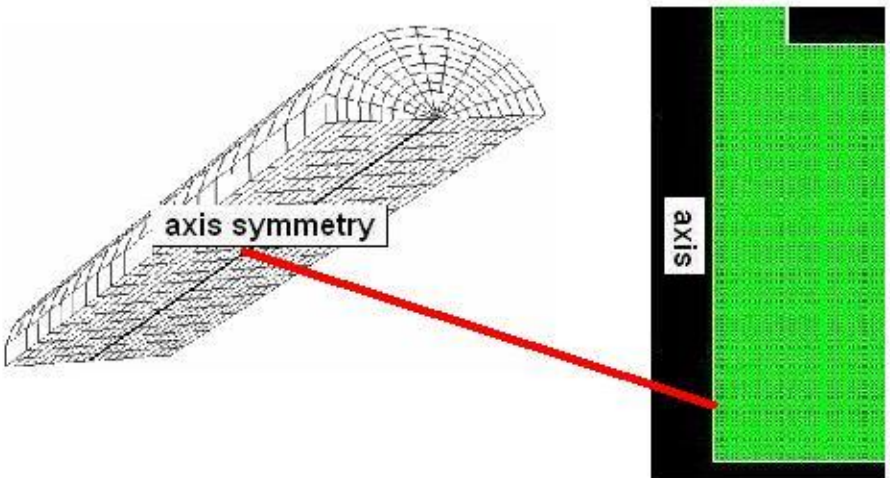

Figure 3.4. Mesh generation with axis boundary condition

3.3.3. Computational Details

- **Convergence Criteria**

Convergence is the property of a numerical method to produce a solution which approaches the exact solution as the grid spacing, control volume size or element size is reduced to zero.

The computations require nearly 50.000 iterations for satisfactory convergence (velocity, continuity, energy, k, ε, ω) for a 2-D jet domain. The iterations continue while the all the residual error is smaller than e-08.

In according to Fluent 6.3 Users Guide, the unscaled residual error R^{Φ} is computed by FLUENT as shown in below.

$$R^{\Phi} = \sum_{cellsP} \left| \sum_{nb} a_{nb}\Phi_{nb} + b - a_P\Phi_p \right| \tag{3.20}$$

Where Φ is general variable, a_p is center coefficient, a_{nb} are the influence coefficients for the neighboring cells, b is the contribution of the constant part of the source term and of the boundary conditions.

Generally, it is difficult to judge convergence by examining the residuals defined by Equation 3.20 since no scaling is employed. FLUENT scales the residual using a scaling factor representative of the flow rate of Φ through the domain. This scaled residual is defined as

$$R^{\Phi} = \frac{\sum_{cellsP} \left| \sum_{nb} a_{nb}\Phi_{nb} + b - a_P\Phi_p \right|}{\sum_{cellsP} a_P\Phi_P} \tag{3.21}$$

For the momentum equations the denominator term $a_p\Phi_p$ is replaced by a_pv_p, where v_P is the magnitude of the velocity at cell P.

For the continuity equation, the unscaled residual for the pressure-based solver is defined as

$$R^C = \sum_{cellsP} \left| rate\ of\ mass\ creation\ in\ cell\ P \right| \quad (3.22)$$

The pressure-based solver's scaled residual for the continuity equation is defined as $\frac{R^C_{iteration\ N}}{R_{iteartion\ 5}}$. The denominator is the largest absolute value of the continuity residual in the first five iterations.

- **Under Relaxation factor**

The constant under-relaxation factors are shown in the following.

- Pressure = 0.3
- Momentum= 0.7
- Energy = 1
- Turbulence Kinetic Energy = 0.8
- Turbulence Dissipation Rate = 0.8

- **Run-Time**

For the present study, convergence criteria for continuity, momentum and energy equation are monitored during the iterative solutions and their absolute criteria for convergence is equal to 1e-08.

The computational run-time is taken nearly 30 minutes per each run by using a computer that has 1.86 GHz processor and 2 GB ram.

CHAPTER 4

EXPERIMENTAL SET UP

4.1. Jet Parameters

Establishing a water jet impingement facility generally consists of determining a jet diameter, jet-to-plate distance, jet diameter-to-radial distance, flow rate of the water and design of peripheral mechanisms such as the traverses for hotwire anemometers and/or other probes and heater assembly. Entire design must be performed with leakproofing in mind. A 3-D solid design and computational fluid dynamics software were used as design tools during various design steps. Related analysis and material selection are presented in the following.

Determination of jet impingement parameters affects the basic dimensions of the experiment set-up. Parameters are the ratio of radial distance from jet nozzle axis to the diameter of jet (X/D), the ratio of axial distance from nozzle exit to impingement plate to jet diameter (Z/D) and Reynolds and Strouhal numbers.

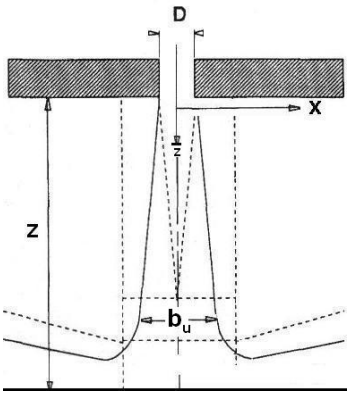

Figure 4.1. Jet parameters

The first two objectives of the finding the radial and axial dimensions of the setup (X and Z) are accomplished by literature survey. It can be seen that for radial distance X greater than about 7 nozzle diameters, the local heat transfer coefficient is independent of the nozzle to plate spacing (Z) as seen in Figure 4.2 (Goldstein et al. 1986). For this reason, X dimension is chosen to be greater or at least equal to 7 nozzle

diameter. Suitable range for Z/D ratio is chosen such that the interesting second peak of heat transfer coefficient as shown in Figure 4.2 can be observed; therefore this ratio is chosen between 2 to 10. The nozzle diameter is assigned to be 10 mm in order to keep Reynolds number near 10^4 with manageable jet exit velocity (near 1m/s). These dimensions allow us to large enough Z distance so that hot wire anemometer and other measurements can be performed with ease. Thus Z dimension is chosen such that it can be adjusted between 20 mm and 100 mm.

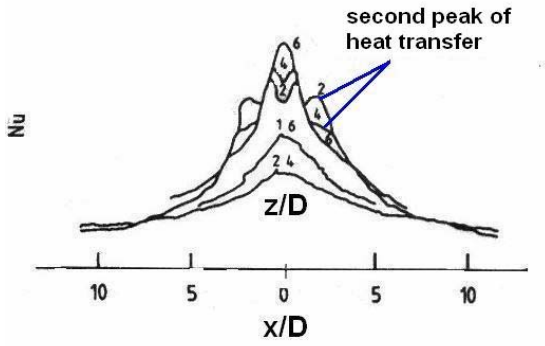

Figure 4.2. Effects of jet parameters on heat transfer coefficient (Source: Gardon and Carbonpue 1962)

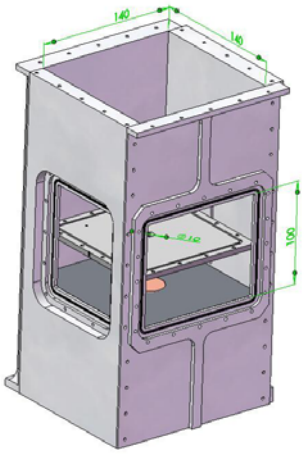

Figure 4.3. Main dimensions of jet setup

After X and Z values were assigned, main dimensions of the jet impingement setup occurs to be as shown in Figure 4.3. Shortly, the reservoir of the jet is X/D=14x14 (140 mm * 140 mm), and the maximum working impingement range is Z/D=10 (100 mm). Two windows that are designed are for visualization for all Z range.

Turbulence increases mixing of coolant fluid and therefore the heat transfer coefficient. For this reason turbulent flow is usually preferred at many jet applications where more heat transfer is the goal. This is also the reason why in this thesis turbulent flow region (near Re=10^4) is chosen for the study. Water is preferred as coolant because of its high specific heat and thermal conductivity than other coolant fluids. Note that, when the temperature of water is 20^{o}C, jet velocity has to be 1 m/s in order to keep the Reynolds number near 10000.

4.2. Working Principles of the Experimental Set-up

The studied type of the impinging jet is called confined-submerged jet. This type of the jet is preferred over others because of its superior heat transfer characteristics in a compact jet design. However, leak proofing the jet design with its moving probe mechanisms is always a challenge. Water sealants must be used where necessity arise.

There is a standpipe used for regulating the flow upstream of nozzle. It also helps the jet exit velocity profile to become uniform. In addition to this, the flow is taken out from the perimeter of jet room. Width of this outlet is 3 mm in cross section all around the standpipe (Figure 4.4-a). The outflow should be axisymmetric in order not to affect jet symmetry. After the flow passes through these flow paths, it is being collected in the outflow region and then taken out of the system (Figure 4.4-b). The velocity of the flow at the 3 mm cross section of outflow path is found to be very low (0-0.07 m/s) by computational fluid dynamics analysis (Figure 4.5). Namely, the standpipe divides system into two regions as active jet region and passive outflow region.

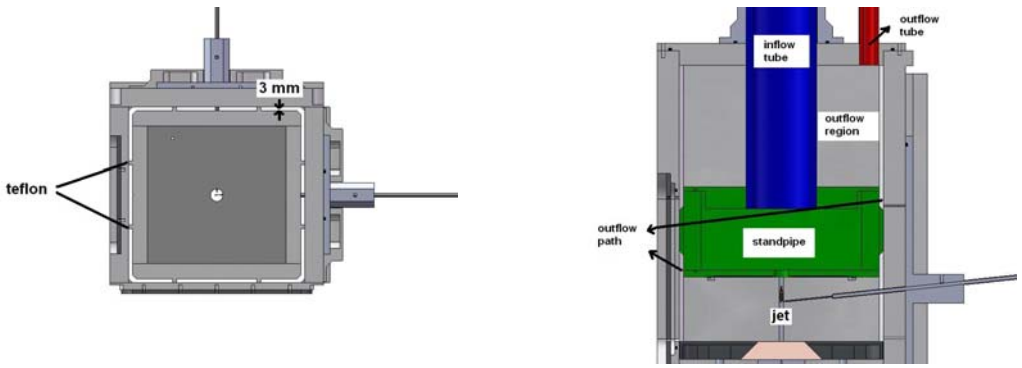

(a) (b)

Figure 4.4. Top and side views of the jet set-up

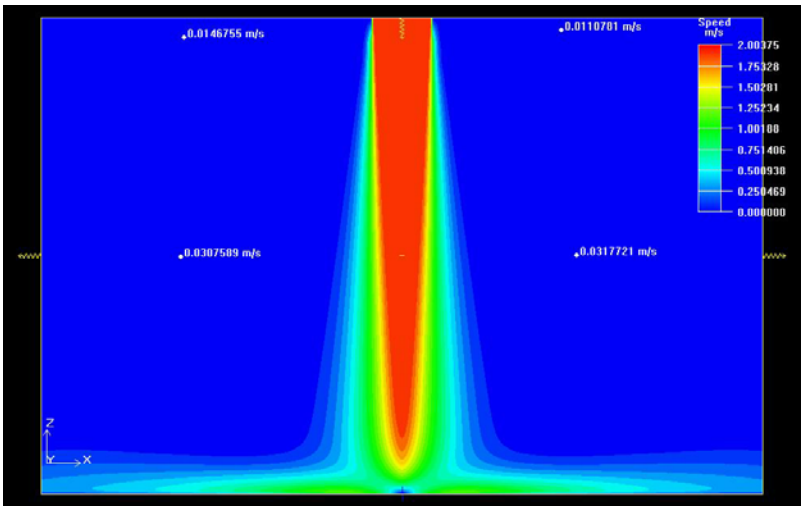

Figure 4.5. A typical velocity distribution of the impinging jet flow. Note the very small velocities at the upper corners where out flow has been taken.

An orifice type nozzle with sharp corners is used assembled such that if it is found to be necessary to replace the nozzle in future, it can be changed easily, Figure 4.6-a. Centering of the standpipe is achieved by rubber ribs placed at the perimeter of the outer surface of the standpipe walls as seen in (Figure 4.6-b and 4.6-c). The nozzle to plate spacing (Z) is adjusted by moving the standpipe as shown in Figure 4.7.

(a) The nozzle plate

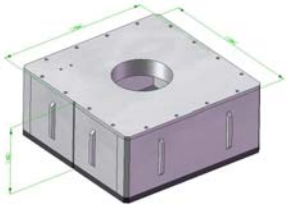

(b) The standpipe

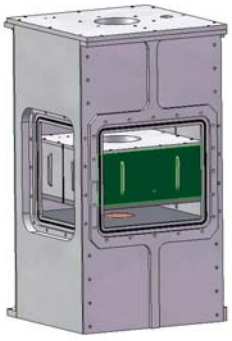

(c) Position of the standpipe in the set-up

Figure 4.6. Design of the standpipe and nozzle

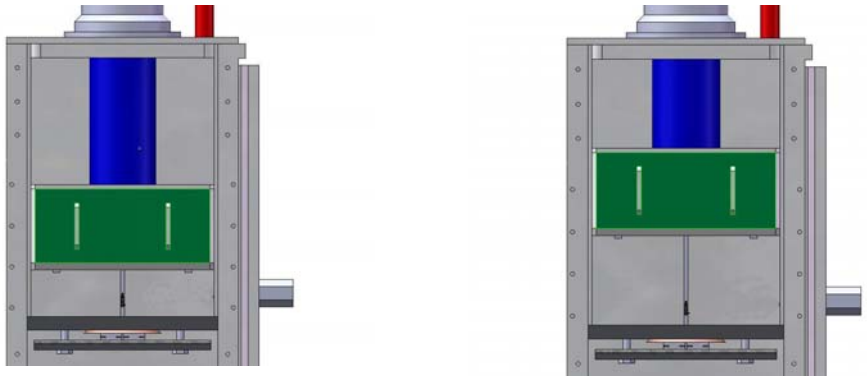

(a) Z / D = 2 (b) Z / D = 6

Figure 4.7. Adjustment of Z/D by moving the standpipe

4.3. Travers Mechanism For Hot-wire Anemometer

There is a main design problem that needs to be solved in hot-wire traverse mechanism. It is that hot-wire has to be able to be moved in two dimensions (x, z) without causing any water leak.

As shown in Figure 4.8.a, slot let hot-wire move in two dimensions and is machined on the two sides of the container. A flat plate is designed to fix the hot wire in position by an angled slot (Figure 4.8.b). It is able to slide on the container thus hot-wire is positioned at the required point. An accurate and precise motion is being provided by micrometer measurements. Once the hot-wire is positioned, it is fixed by a set screw and also o-ring is used between the slotted body and the sliding-plate for leak proofing. As for the last step of the design of the hot-wire traverse mechanism, a part is required to push the sliding-plate on to the container so that to secure leak proofing (Figure 4.8.c). This is done by a sheet-metal springs. This part has a built in flange to be assembled on to the main body. Thereby the slings-plate attached with hot-wire can easily move without any leakage (Figure 4.8.d).

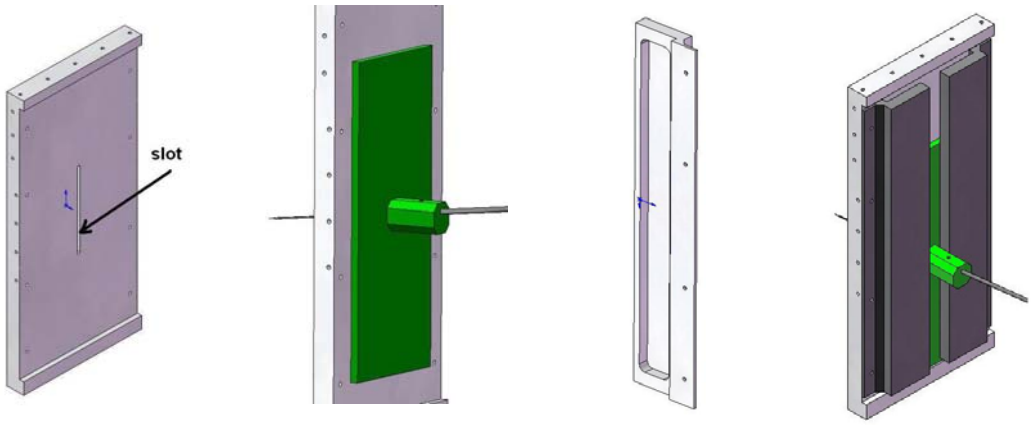

Figure 4.8. Mechanism of hot-wire anemometer

4.4. Heater Assembly

One of the main components of the jet impingement setup is the heater group. This group provides the required heat flux. Four resistance heaters are chosen to obtain 16 W/cm^2 of heat flux and each one is able to dissipate 100 W power (Figure 4.9).

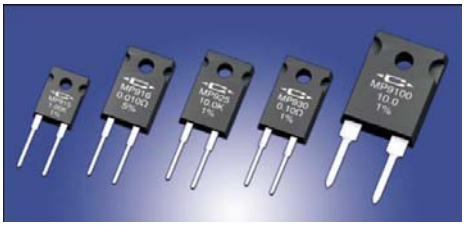

Figure 4.9. Film Resistances
(Source: MP 9100, Caddock Electronics)

With reference to: [1]150 W from cross-section of 9 cm^2 is subjected to jet flow. Therefore, as shown in Figure 4.10-a, these resistances are assembled under a flat-top-conical copper part whose conductivity is about 380-401 W/mK. An insulator is covered all around the copper part and resistances to prevent from heat loss (Figure

1-Q ^{II} = Q / A = 16 W/cm^2 (objected heat flux)
Q = 150 W (apply heat)
A = 150 / 16= 9 cm^2 (required heat flux surface) (Figure 4.13-a)
A= π * r^2 → r = 17 mm (radius of heated surface)

4.10-b). The copper part is pressed onto the center of the impingement plate which is made from nickel-chrome alloy whose conductivity is about 12 W/mK, as seen in Figure 4.10-c. Heater assembly is shown in Figure 4.10-d and the entire assembly can be seen in Figure 4.14.

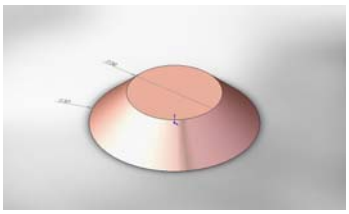

(a) Copper carrier

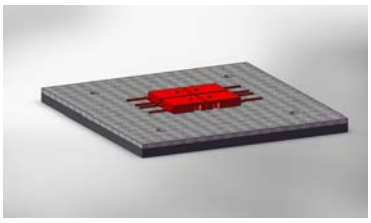

(b) Resistances and Insulator

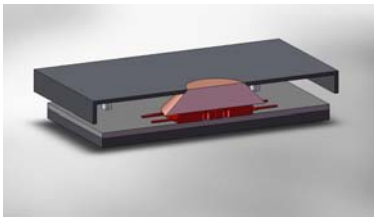

(c) Cross-section of heater group

(d) Assembly of heater group into jet set-up

Figure 4.10. The heater group

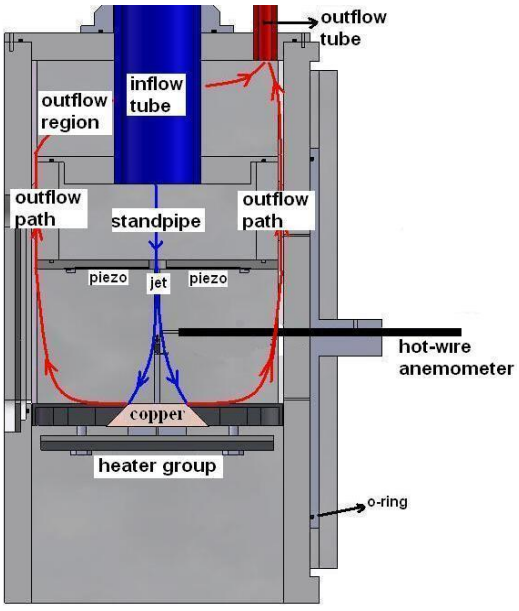

Figure 4.11. Cross section view of the complete jet impingement setup

4.5. Experiments with Air Jet

There are two kinds of experiments were performed with air; flow visualizations and pitot tube measurements and two jet types are used as impinging and free jets. They were the first experiments performed before the water setup was ready. Pitot tube and micro-manometer (Figure 4.12a - 4.12b) are used for velocity measurements. Pitot pressure measured by manometer is converted to the velocity by Bernoulli equation. Velocities for each 1 mm interval in the direction of x are measured at designated 'z=const.' cross-sections. A CCD camera (Figure 4.12d), a small laser with 532 nm wave length and power of 100 mW (Figure 4.12c) and cylindrical lens for creating a laser light sheet are used for flow visualization.

(a) Manometer

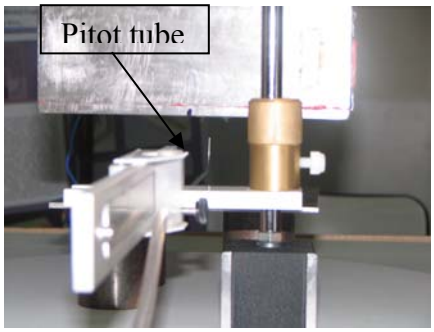

(b) Pitot Tube

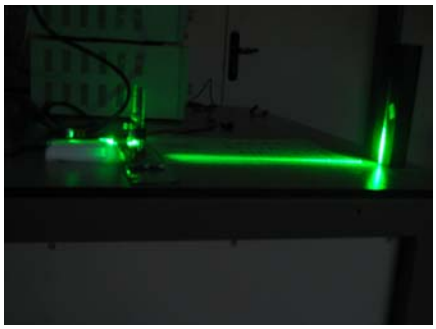

(c) Laser

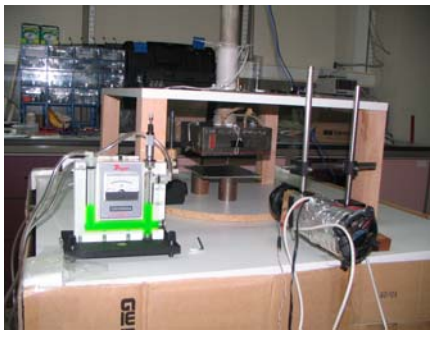

(d) Camera and Experimental set-up

Figure 4.12. Experimental set-up for air jet

4.6. Experiments with Water Jet

The water is used as fluid in these experiments. The jet velocity of 1 m/s is provided by free falling of the water from an elevated container. A Schematic view of the experimental set up for water jet is shown in Figure 4.13. Jet velocity is kept constant by keeping the height of the free surface of water column steady in the water tank (4). Required water is fed from supply tank (1) by a pump (2). While flow visualization experiments are running, the water is emptied to drainage (11) to keep the system clean from flow marker (regular milk for this case).

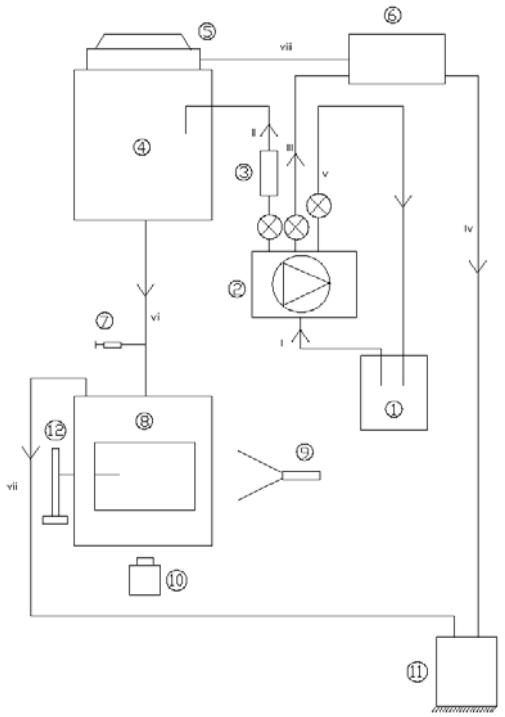

1. Supply Tank
2. Pump
3. Flow meter
4. Water tank
5. Loudspeaker
6. Amplifier
7. Milk Injection
8. Jet set-up
9. Laser
10. CCD camera
11. Drainage
12. Hot-wire

i. Supplying pump line
ii. Supplying water tank line
iii. Amplifier cooling system line (in)
iv. Amplifier cooling system line (out)
v. Pump short cut line
vi. Jet supplying system line (in)
vii. Jet supplying system line (out)

Figure 4.13. Experimental set-up for water jet

Briefly, following is the description of the flow diagram. The water taken from the supply tank by the supply line (i) is divided into three lines at the exit of the pump by the fittings. One of those goes to water tank by line (ii) whose flow rate is measured by a flow meter (3) since it supplies water directly to the jet set-up (8). Another line is for the cold plate of the amplifier (6) and carried by the line (iii). Line number (iv) carries away the heated water from the amplifier. The line number (v) is the short-cut between pump and supply tank thus it prevents the pump from overloading. The water is perturbed by the sound waves from a loudspeaker (5) which is then transmitted to the

jet set-up by the line (vi). The milk is used as a flow marker for flow visualization purposes due to its closely matching density and common availability is mixed with the water at the injection apparatus (7). After water jet impinges to the plate, it exits through the line (vii) to the supply tank or to the drain.

A small power Laser (9) is used to illuminate the visualization plane of the jet nozzle (usually the center plane). A CCD camera (10) which looks perpendicularly to the illuminated plane acquires images of the jet flow.

Hot wire anemometer is delivered to the jet set-up with a traversing mechanism (12). This mechanism makes hot wire to traverse horizontally and vertically therefore two dimensional plane can be completely measured. All of these sub-instruments' photos are shown in following figures.

Supply tank (Figure 4.14) is used for storing enough clean water for experiments. It has three filters installed the supply tank to clean the water. Free falling of water for the jet setup starts from the water tank (Figure 4.15). There is a woofer mounted on top of the water tank that generates sound pressure waves above the water tank. The steadiness of the free surface of the water was observed for at least 5 minutes before each experiment to make sure it does not change.

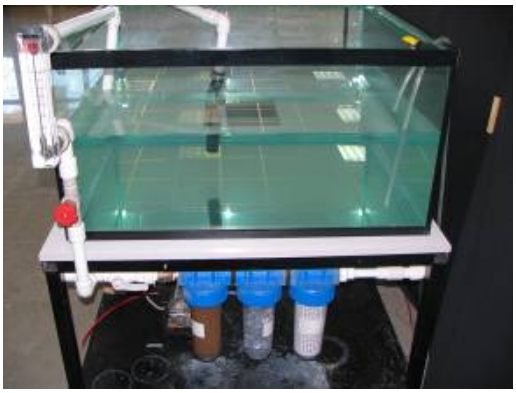

Figure 4.14. Supply Tank

Figure 4.15. Water Tank

Perturbation of the flow is obtained by a loudspeaker (Figure 4.16) that is 11'' in diameter and with a working range of 25 Hz-2500 Hz with total of 450 W. Loudspeaker is drived by an amplifier shown in Figure 4.17. It is fed by a sinusoidal wave by a function generator seen in Figure 4.18. The amplifier is needed to be cooled rigorously

and therefore a water cooled cold plate is assembled under the electronic circuit. Required water is obtained from the supplied tank as mentioned before.

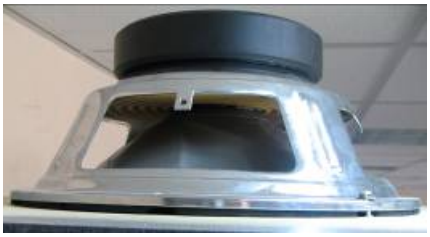

Figure 4.16. 11'' diameter, 450W loudspeaker to produce sound pressure waves

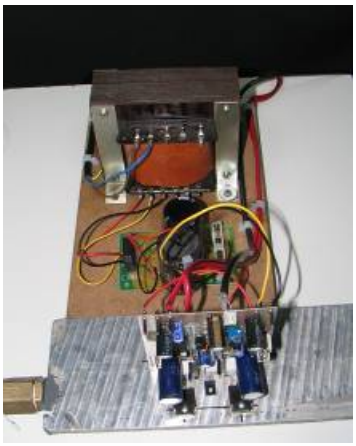

Figure 4.17. The home made amplifier and its cold plate

Figure 4.18. Function generator, oscilloscope, power supplies and computer

Hot wire anemometer, assembled to the traverse mechanism as shown in Figure 4.19 for moving through x and z axis easily, is used at velocity measurement experiments. Traverse mechanism is moved horizontal and vertical by two trapezoidal screws manually. The mechanism can be adapted to automation in future by driving these screws by control motors. Hot wire anemometer is centered in the test section by a cylindrical brass tube at the entrance the jet set-up. Two o-rings (Figure 4.20) are used at the brass tube to prevent leaks while hot wire anemometer is moving.

Displacement of hot wire sensor is measured by a comparator (Figure 4.19) that has 10 mm range and 0.01 mm measurement scale.

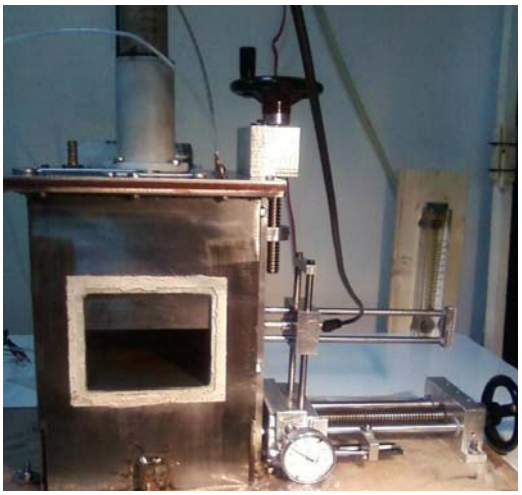

Figure 4.19. Traverse mechanism assembled on the jet set-up and its comparator

Figure 4.20. Brass tube and o-rings

In flow visualization, the milk is used as a marker because its density is almost same to density of water. The visualizations are taken by using CCD camera shown in Figure 4.21. The middle of the test section is illuminated by a laser light. Laser beam is sent through a cylindrical lens to create a light sheet so that to illuminate only 2D cut out from the flow.

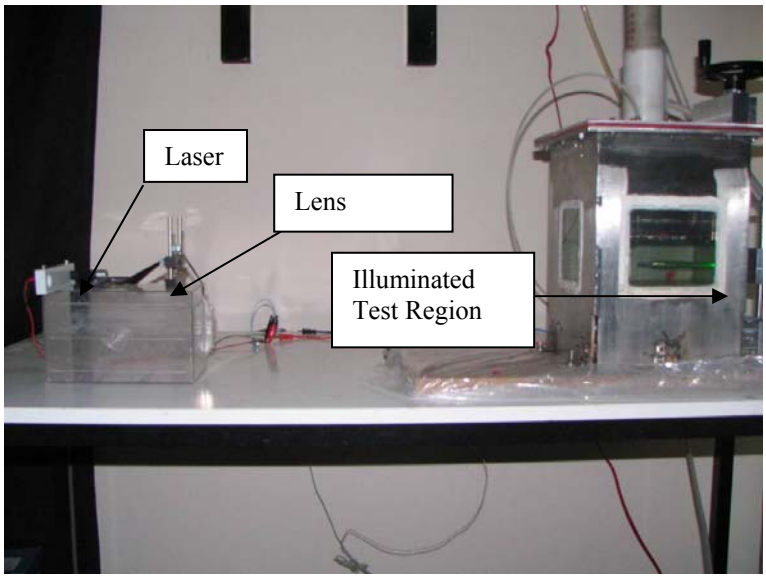

Figure 4.21. The CCD camera and the laser setup.

A single hot wire sensor is used to analyze the turbulence intensity and velocity distribution of the jet flow due to their sensitivity. The sensor's dimensions are 25.4 microns diameter and 510 microns length. Its mechanical dimensions are shown in Figure 4.22.

Hot wire anemometers use a very fine wire (on the order of several micrometers) electrically heated up to some temperature above the ambient. Air flowing past the wire has a cooling effect on the wire. As the electrical resistance of most metals is dependent upon the temperature of the metal, a relationship can be obtained between the resistance of the wire and the flow velocity. Several ways of implementing this exist, and hot-wire devices can be further classified as CCA (Constant-Current Anemometer), CVA (Constant-Voltage Anemometer) and CTA (Constant-Temperature Anemometer). The voltage output from these anemometers is thus the result of some sort of circuit within the device trying to maintain the specific variable (current, voltage or temperature) constant. Additionally, PWM anemometers are also used, wherein the velocity is inferred by the time length of a repeating pulse of current that brings the wire up to a specified resistance and then stops until a threshold "floor" is reached, at which time the pulse is sent again. Hot-wire anemometers, while extremely delicate, have extremely high frequency-response and fine spatial resolution compared to other measurement methods, and as such are almost universally employed for the detailed study of turbulent flows, or any flow in which rapid velocity fluctuations are of interest.

Sensors are calibrated in the same experimental against a pitot tube and/or measured flow volume. 1.5 mm inner diameter pitot tube is located near the center of the jet at 0.6 D along the z direction. In this location, flow is still laminar regime and turbulence intensity is nearly 1% so it is appropriate for pitot tube measurements. Jet velocity profile is shown in Figure 4.23 and is determined by pitot tube. This profile shows that jet core is uniform at the center of the nozzle. Diameter of this uniform region is equal to diameter of jet nozzle, 10 mm. Therefore, this region has enough area to room both hot wire sensor and pitot tube simultaneously. The configuration of hot wire sensor and pitot tube together during a calibration run is shown as Figure 4.24.

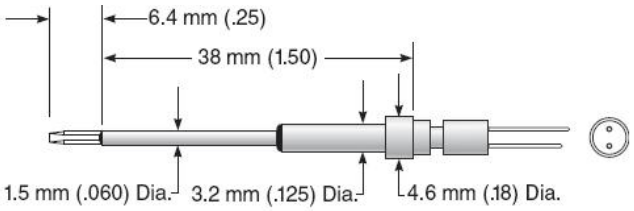

Figure 4.22. Hot wire sensor

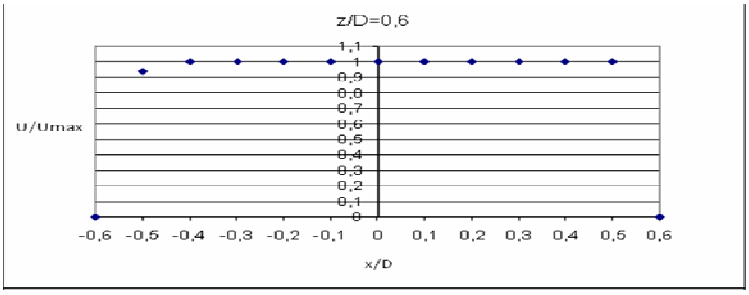

Figure 4.23. Velocity profile at z=0,6D measured by a pitot tube

Figure 4.24. Settling of hot wire sensor and pitot tube for calibration

Bridge voltages of hot wire anemometer and velocity profiles are correlated with 4th degree polynomials. One of them is shown in Figure 4.25.

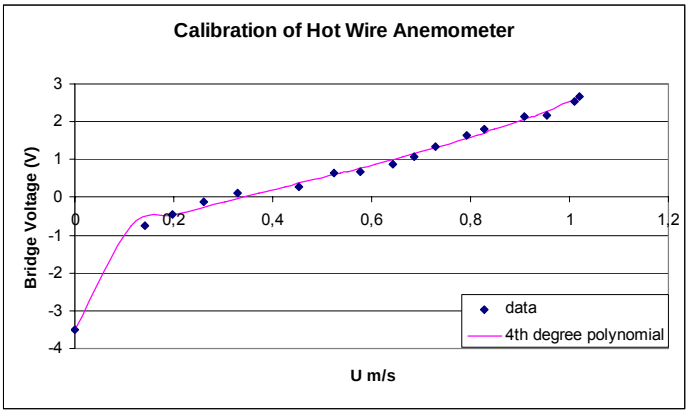

Figure 4.25. 4th degree polynomials trend line for calibration (Gain= 5, Offset = 2.14)

Jet velocity profile and turbulence intensity are measured for each 1 mm space through the x axis at z/D=0.6, 2, 3 and 5.4. Each data is logged at a rate of 1 kHz for 8 seconds. Turbulence intensity is defined as the following.

$$\text{Turbulence Intensity: } TI = \frac{\sqrt{\frac{1}{3}\left(u_x'^2 + u_y'^2 + u_z'^2\right)}}{\bar{u}} \qquad (4.1)$$

Firstly, flow visualization experiments should be run thus general flow characteristics (jet spreading, turbulence structure etc.) can be examined. For these experiments, Strouhal number that is correlated with frequency is selected some values between 0.25 and 1. Following that, hot wire measurements are performed with different amplitudes at the arranged Strouhal numbers from the visualization experiments. The peak to peak amplitudes of the sinusoidal signal sent from the function generator to amplifier are 0.5, 1 and 1.5 V in order to see how to affect jet flow characteristics.

One single wire sensor is used so the measured velocity is a resultant of x and z components of the velocity vector (U_x and U_z). Measured velocity (U) is then illustrated by the following equation.

$$U = \sqrt{U_x^2 + U_z^2} \tag{4.2}$$

4.7. Heat Transfer Coefficient Measurements

Required heat flux is obtained by using four precision resistances assembled under the copper carrier. Four thermocouples are positioned at the centerline of the copper carrier. They are located at x/D=0, 0.5, 1 and 1.5. The thermocouples are placed near the impinging surface by 2mm holes on the copper carrier as seen in Figure 4.26. They sense the temperature from only 2 mm below the impinging surface and inside of the copper. We assume that the surface temperatures and the thermocouple temperatures are equal because of high thermal conductivity (k) of copper. Another thermocouple is used for measuring the water inlet temperature. The measured surface temperature and the inlet temperature are used for calculation of the heat transfer coefficient (h) and Nusselt number (Nu) of the jet. Nu and h is described as

$$h = Q_{net} / A * \Delta T \tag{4.3}$$

$$Nu = h * D / k_{water} \tag{4.4}$$

Where,

Qnet: $Q_{total} - Q_{loses}$

A: Surface of heat subjected

ΔT: Difference between surface temperature and inlet water temperature

D: Diameter of the jet

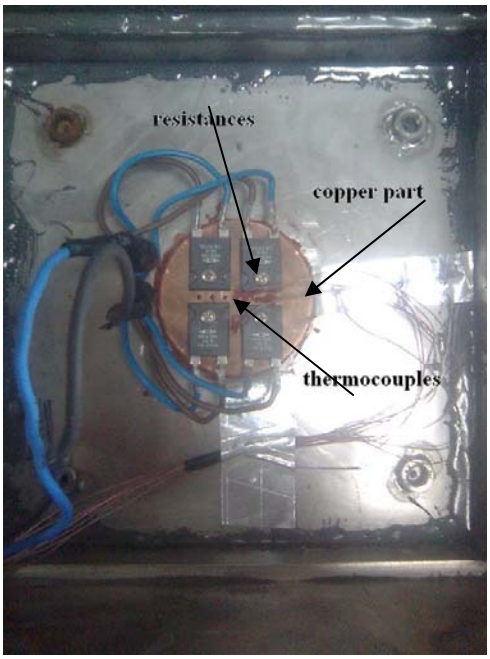

Figure 4.26. Heater group (bottom view of the jet set up)

Heat losses from the system are measured by a calibrated insulator setup as seen in Figure 4.27. All of the heater group parts are insulated by an insulator and covered by the MDF material whose conductivity (k_{MDF}=0.2231 W/mK) is measured by a automated measurement device KEM QTM 500. Single thermocouple is fix on each ten surfaces and of the MDF box (five inner and five outer surfaces) except at surface looking into the heater group. Thus temperature differences between two sides (ΔT_{wall}) of the MDF walls are measured. Then the heat loss (Q_{loses}) from all surfaces is easily calculated by the conduction equation as

$$Q_{loss} = \sum_{i} \frac{k_{MDF}.A_i.\Delta T_i}{\Delta X} \tag{4.5}$$

Where A_i and ΔT_i are area and the temperature difference of the corresponding wall and the ΔX is the thickness of the MDF walls which is 22mm.

Figure 4.27. MDF Covering, insulator and thermocouples for heat loses measurements

CHAPTER 5

RESULTS AND DISCUSSION

5.1. Numerical Results

Center velocity (U_c) along the z direction is determinative on spread rate and core length results therefore it is selected as a dependent parameter for the mesh independence checks. U_c values are graphed for different mesh numbers in Figure 5.1. As shown in this figure, U_c values are independent from the mesh number over 3000 for a 2D numerical domain.

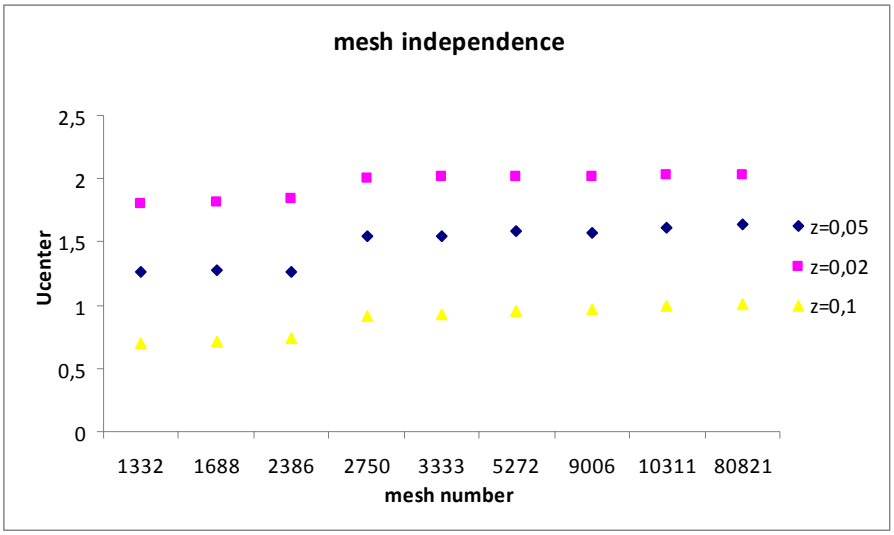

Figure 5.1. Mesh Independence

A common definition of the end of the core region is the point where U_{core} = 0.95* U_c. A core length of nearly six nozzle diameters (D) for turbulent Reynolds number has been suggested by Gautner et al.(1970). Our computations seen in Figure 5.2 are in a somewhat agreement, z = 5.33 *D.

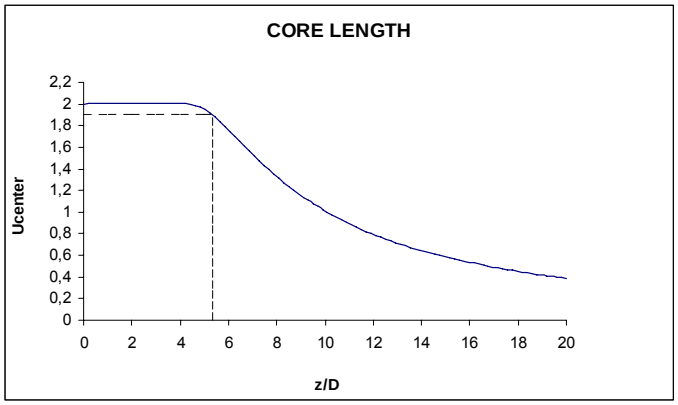

Figure 5.2. Core Length

Jet half width (b_u) is a very commonly used parameter to compare different studies. An analysis by Schlichting et al (1968). showed that the fall of the centerline velocity and the jet half width will be directly proportional to the axial distance from the end of the potential core. According to this analysis in free turbulent flow the jet problems are a boundary layer nature. Downstream of the potential core, free jet zone occurs in z direction and spread rate is assumed to be constant for this region.

Chen and Jaw et al. (1998) reported that the spread rate changes between 0.0713 and 0.086 according to various experimental data. The spread rate was found by our computations as 0,123, over estimating the experimental results. The spread rate shown in Figure 5.3 decreases sharply until the free jet region and after that its value is almost constant.

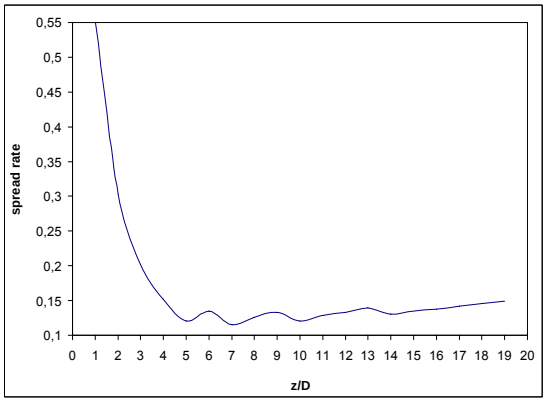

Figure 5.3. Spread Rate

Figure 5.4 contains a comparison of jet velocity profiles at z=10D for k-ε and k-ω turbulence models and Tollmein (1931) and Reichart-Goertler (1942) analytical

solutions. Short hand on the legend shows that jet was a free jet (FJ), for k-e and k-ω turbulence models. All the other models seem to agree cross the jet models agree with the Tollmiens analytical solution up to x= $b_{u1/2}$.

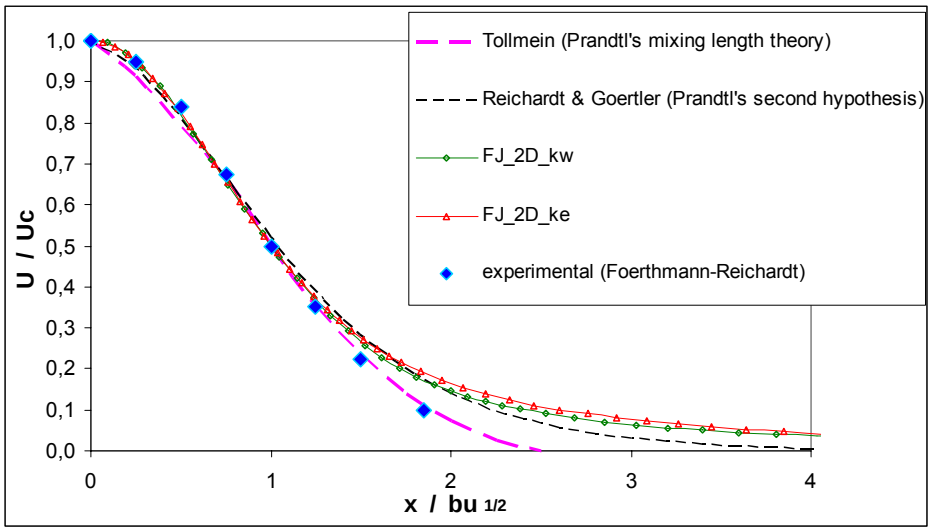

Figure 5.4. Velocity distribution in a free turbulent jet at z/D=10.

A comparison between various solutions (analytical and numerical) and experiments indicates that solutions obtained from Prandtl's 2nd hypothesis (see Chapter 2) matches the experiments in the core of the jet whereas solutions obtained from Prandtl's mixing length theory matches them very well in the outer skirts of the jets. As for the computations, all of the models seems to agree well with the experiments up to x=$b_{u1/2}$. N. Zuckerman and N. Lior et al. (2005) reported that k-ω model predicts of jet analysis better than k-ε models because the user can fully specify the turbulence conditions at the wall, unlike in the k-ε model. A similar comparison with an experimental data is shown in Figure 5.5 with a different scaling (x/z) where z is the jets center axis and it indicates that k-ω turbulence models is indeed in the best agreement with the experimental results.

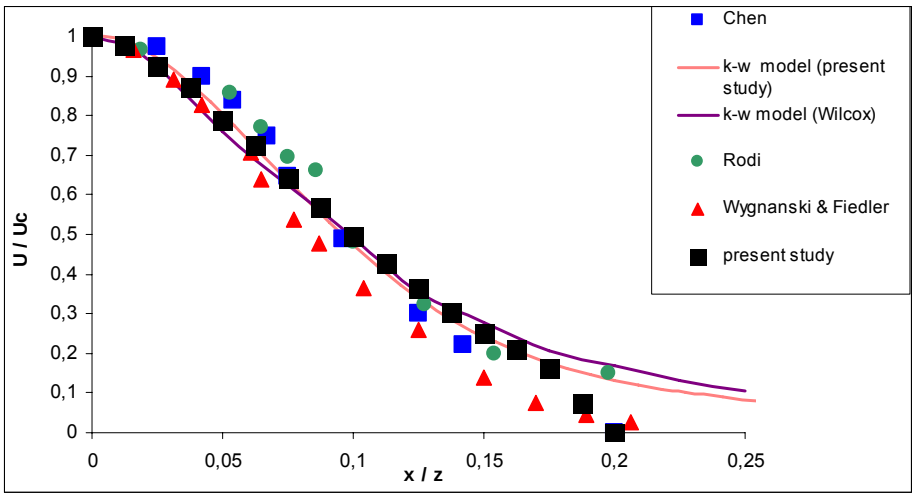

Figure 5.5. Comparison Turbulence models with numerical and experimental data

Numerical solutions for heat transfer at a jet impingement were also investigated. These were compared with Yan (1993), Baughn and Shimizu's (1989) experimental data and also k-ε turbulence modeling of Behnia. As shown in Figure 5.6 and 7, k-ω is a better predictor than k-ε according to experimental data because it can analyze better of the turbulent length scale and flow properties in the wall jet, both in sublayer and logarithmic region, without the need of damping functions as k-ε does.

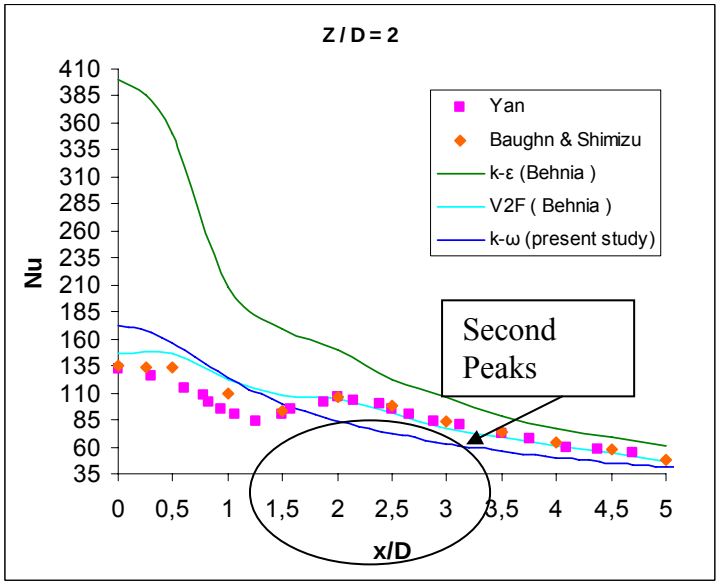

Figure 5.6. Distribution of local heat transfer coefficient for Z/D=2 and Re=23000

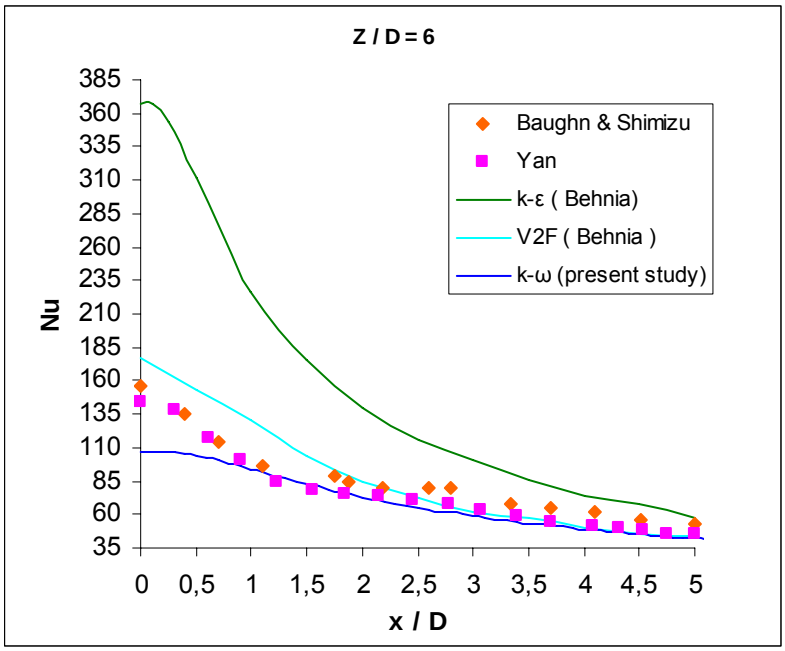

Figure 5. 7. Distribution of local heat transfer coefficient for Z/D=6 and Re=23000

However, prediction by the k-ω model is anomalous in magnitude and location of second peak of heat transfer coefficient. Even though experimental data show that it occurs at nearly x/D=2, k-ε and k-ω models can not find this as seen in Figure 5.6. Especially the error of Nusselt number near stagnation point is very high for k- ε (130%). Behnia et. al. (1997) reports that the reason for this inconsistency is the erroneously predicted turbulent kinetic energy near the stagnation zone. This was clearly seen in the Figures 5.8 and 5.9. The figure shows where and how the magnitude of the highest turbulent kinetic energy occurs in the wall jet. It is easily seen why k-ε and k-ω models can not predict secondary Nu maxima; however, V^2F can almost solve position and magnitude of the turbulent kinetic energy correctly. For Z/D=6, there is no second maxima in Nu, as a result of this the k-ω model performs better. The magnitude of the maximum turbulent kinetic energy in the wall jet calculated by the k-ε model are much more than the one by V^2F (0.1 v.s. 0.06 m^2/s^2) data. This is the reason why the k-ε predicts stagnation Nu number with very high errors of 130%.

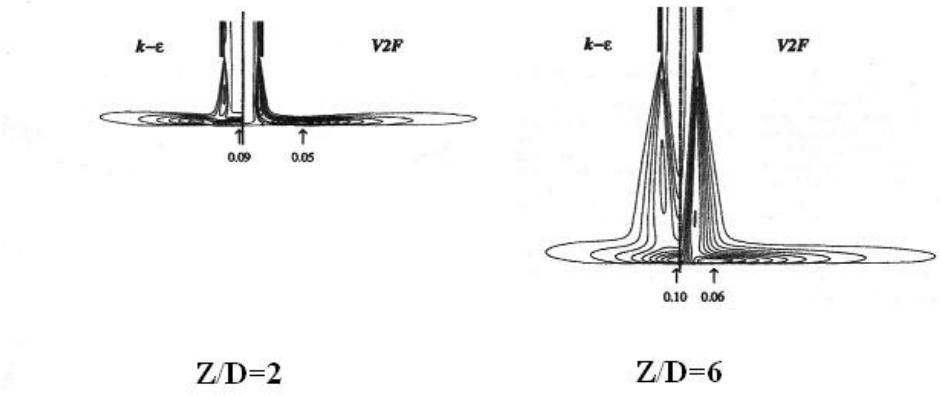

Figure 5.8. Contours of turbulent kinetic energy for Z/D=2 and Z/D=6
(Source: Behnia, et al. 1997)

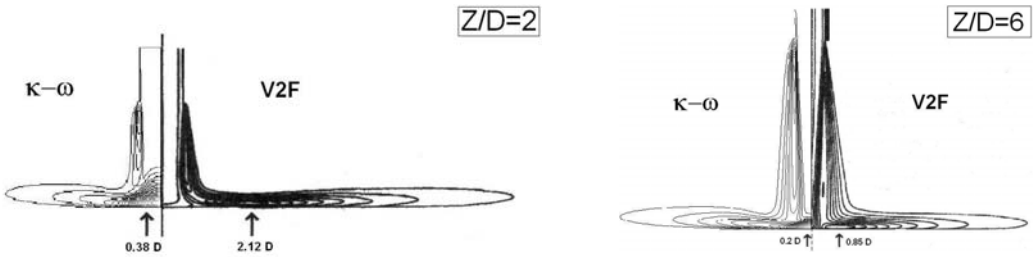

Figure 5.9. Comparison of the turbulent kinetic energies for Z/D=2 and Z/D=6

As shown in Figure 5.10, Schlunder and Gnielinski et al. (1967) found that both the maximum turbulence and the maximum stagnation point heat transfer occurs at Z/D=7.5. Maximum Nusselt number in our k-ω calculations is found near Z/D=3 and decreasing considerably in downstream direction. Although there is a big disagreement in the trend and the peak of Nu, average magnitudes of the Nu is much closer than k-ε model. Nevertheless, Behnia's V^2F model seems to be doing very good job overall. All of these disagreements with the k-ε and k-ω models are due to the fact that near wall turbulent kinetic energy can not be predicted accurately.

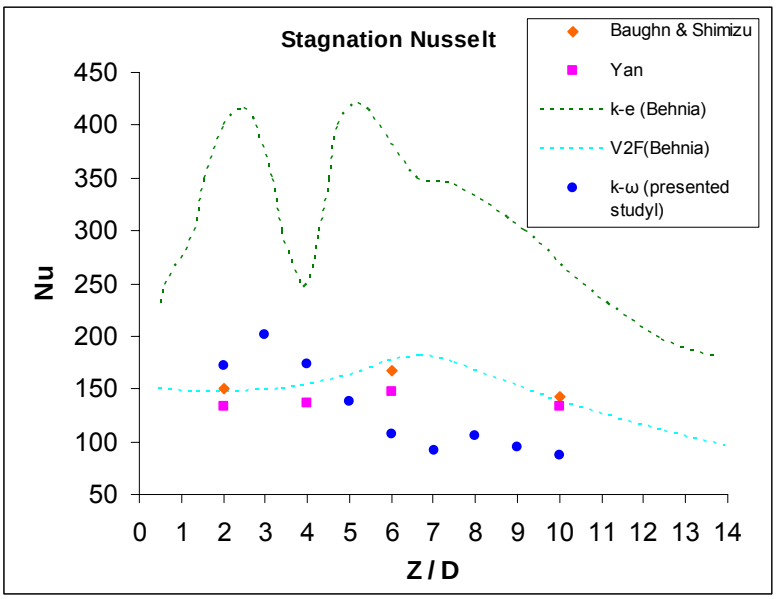

Figure 5.10. Distribution of local heat transfer coefficient for different Z/D

5.2. Experimental Results

5.2.1. Visualization and Velocity Measurements of Air Jet Flow

Visualization experiments of impinging and free jet flows are performed by mixing smoke into the air and illuminating the flow with laser sheet. Aim of the visualization is to observe jet core and shear layers according to variable smoke density. Velocity contours by the numerical analysis of k-ω turbulence model and the flow visualization are compared side by side in Figure 5.11. Jet inlet is positioned on the top center of the image and jet axis line is dividing the image into two parts where on the right constant velocity contours from CFD results and on the left, an ensemble averaged image of smoke visualization are shown. The similarity between two sides of the figure is striking.

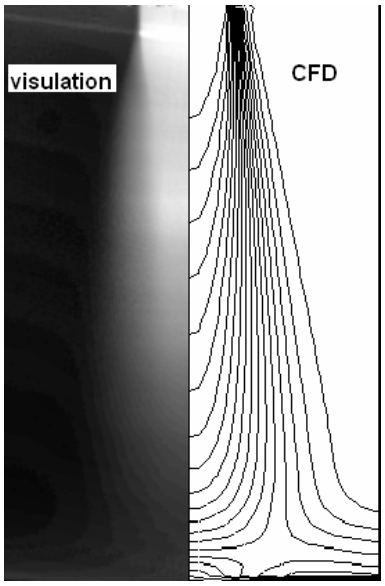

Figure 5.11. Comparison of velocity profile between numerical analysis and flow visualization (Re=10000, turbulence model: k-ω, Z/D=6)

In the Figure 5.12, there are two ensemble averaged images of an impinging (Figure 5.12.a) and a free jet (not impinging) (5.12.b) flow. According to theory, core length of both of these flows should be very close, near z/D=3, and these visualizations, judging from the smoke density, strongly support this finding.

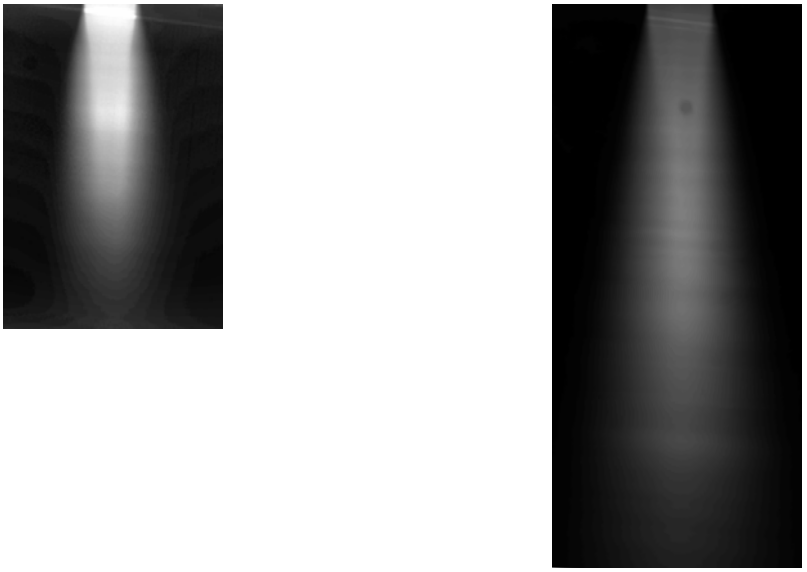

(a) Impinging jet (Z/D=6) (b) Free jet

Figure 5.12. Visualization of impinging and free jet

As shown in Figure 5.5, velocity profiles measured by a pitot tube are compared with other experimental and numerical data to test our consistency. Although all data is

in close range to each other, there are some differences in the details. For example, our data is sharply converged to the zero beyond x/z is greater than 0.15. Most probably it is caused by the shortcomings of the pitot tube measurement in which measurement sensitivity greatly reduces at the small velocities. Other differences are thought to be due to the differences in the boundary conditions.

Perturbation of the jet was first planed to be performed by a vibrating piezoelectric anchored arm of the bender type. It is positioned near the nozzle where the jet shear layer is most sensitive. Comparison of a free jet and a perturbed jet with a piezoelectric bender is performed, however; the maximum possible Strouhal number (*f*D/U*) that could be reached was 0.003 (correspond to 50Hz for the given flow velocity) without destroying the bender itself. This is a very low frequency compared to the flows own instability mechanisms. A smoke visualization comparison is given at Figure 5.13. As expected, there is no significant difference between these two figures.

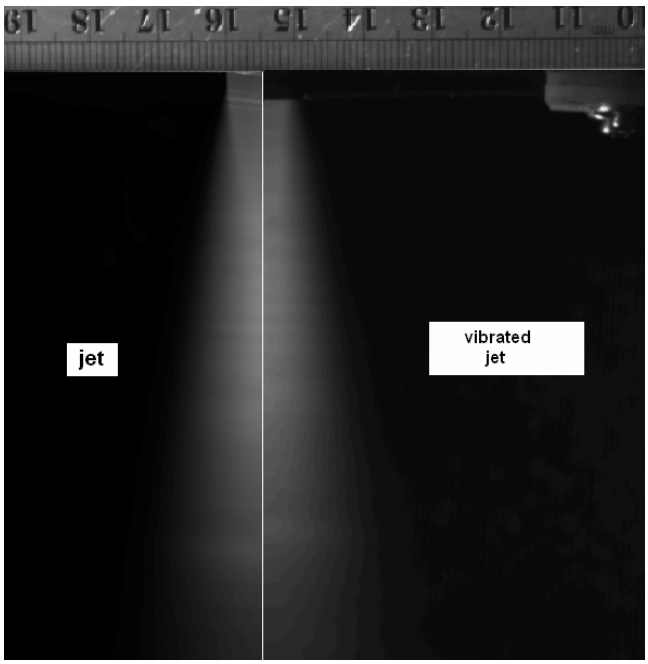

Figure 5.13. Comparison of normal jet flow and vibrated jet at St= 0.003

5.2.2. Visualization and Velocity Measurements of Water Jet Flow

The effects of Strouhal number on the dynamics of the jet flow are the main focus of this investigation. During this study other parameters such as Reynolds number and Z/D=6 are kept constant. Strouhal number is changed be means of changing driving

frequency of which St=0 corresponds to no perturbation on the jet flow. Although perturbations were planned to be applied by piezoelectric bender arms as it was once tried for the air flow and mentioned above, these bender were turned out be very inappropriate for the water applications. Therefore, perturbations are applied with a woofer placed on top of the free surface of the water tank in which flow starts its free fall. Driving signal is supplied to the loudspeaker by a frequency generator and amplified with a homemade 20X amplifier. The amplitude (A) of sinusoidal wave is kept at 2 V at the flow visualization experiments.

The jet flow images are taken by a CCD camera, which takes 20 images per second, for approximately five-second periods. We have obtained ensemble averaged images for the purpose of getting general information about flow characteristics, such as jet width. The averaged images are obtained by using the most clear 25 images instead of using all of them. They are averaged by our Matlab code. Whereas, instantaneous images shows detailed flow structures, for example, coherent structures in the shear layer can only be determined from an instantaneous image. Figure 5.14 shows the differences between instantaneous and average images clearly. These averaged images show jet width and the approximate beginning of turbulence regime from the nozzle lip. However data of hot wire sensor measurements are used for quantitative analyses of jet.

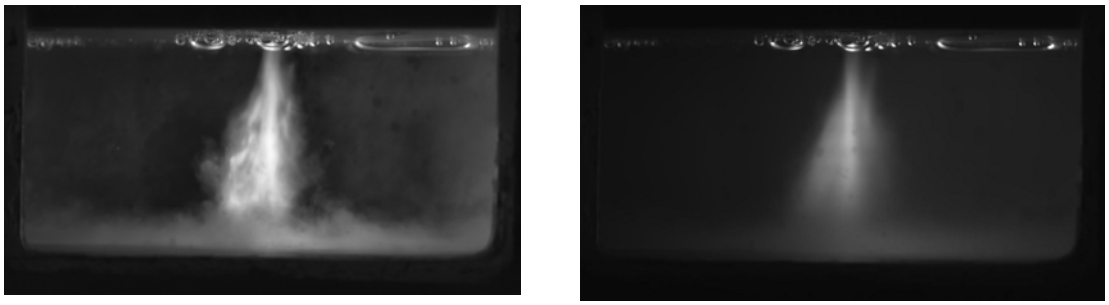

(a) Instantaneous image (b) Average image

Figure 5.14. Instantaneous and average image at St=0.55

Instantaneous images are shown in Figure 5.15 at different Strouhal numbers varied between 0 and 1. It appears that jet flow begins to be affected by the perturbations starting from Strouhal number of 0.25. Jet width increases downstream of z/D=2 where instabilities amplified the most. Especially with the perturbations, increase in the jet width is substantial. Influence of the perturbation is very striking even between St=0 and St=0.25 cases. Perturbing the shear layer with Strouhal numbers between 0.25

and 0.55 cause selective amplification of the coherent structures in the shear layer and therefore significant growth of the jet width. Contrary to this trend, increasing the perturbation frequency beyond 0.55, until to 1.0, does not result in as much growth as the lower Strouhal range. Effectiveness of the Strouhal numbers from 0.25 to 0.55 is also seen similar experiments with free jets in the literature (Crow and F.H.Champagne 1971). More accurate information about the response of the jet width to perturbations can be obtained from ensemble averaged images, Figure 5.16. Although, the final result is the same, the increase in the jet width is more pronounced in these images.

After these analysis, it is seen that near St=0.5 is an effective perturbation on the circular jet in order to increase the width of the jet and therefore the following hotwire measurements are run by keeping the Strouhal number constant at 0.5.

One of the information seek from the hotwire data is to see the effect of the perturbation amplitude. But, it is seen that there is not much of a difference between the different amplitudes tried, which are 0.1, 0.5, 1.5 Volts.

St=0

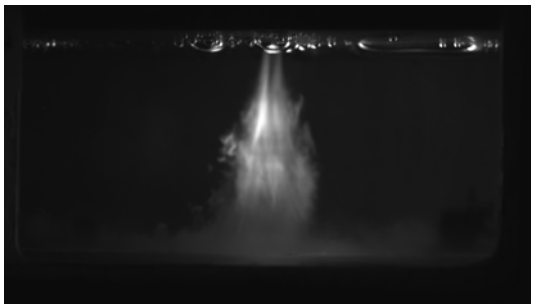

St=0.25

St=0.3

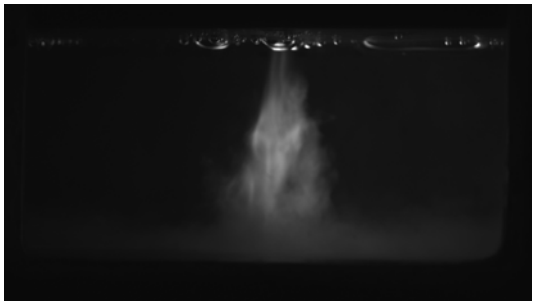

St=0.35

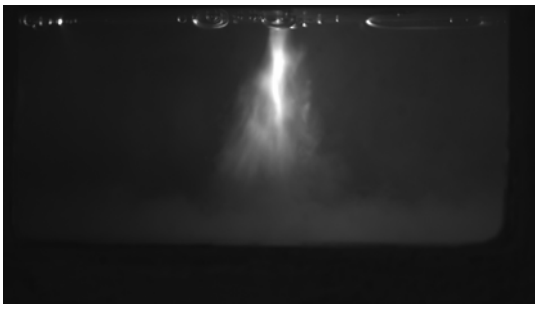

St=0.45

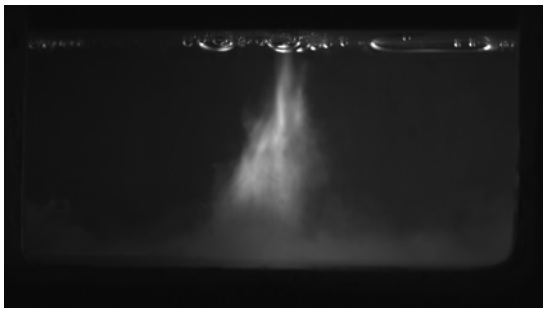

St=0.55

Figure 5.15. Instantaneous images at different Strouhal numbers for Re=10000 Z/D=6

(cont. on next page)

St=0.6

St=0.65

St=0.75

St=0.85

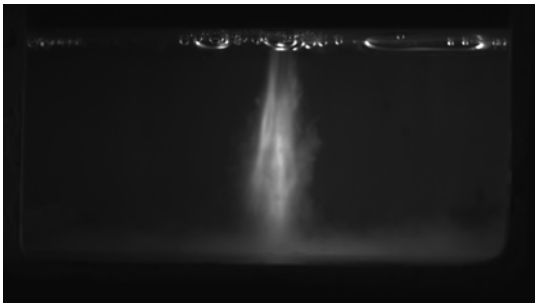

St=1

Figure 5.15. (Cont.)

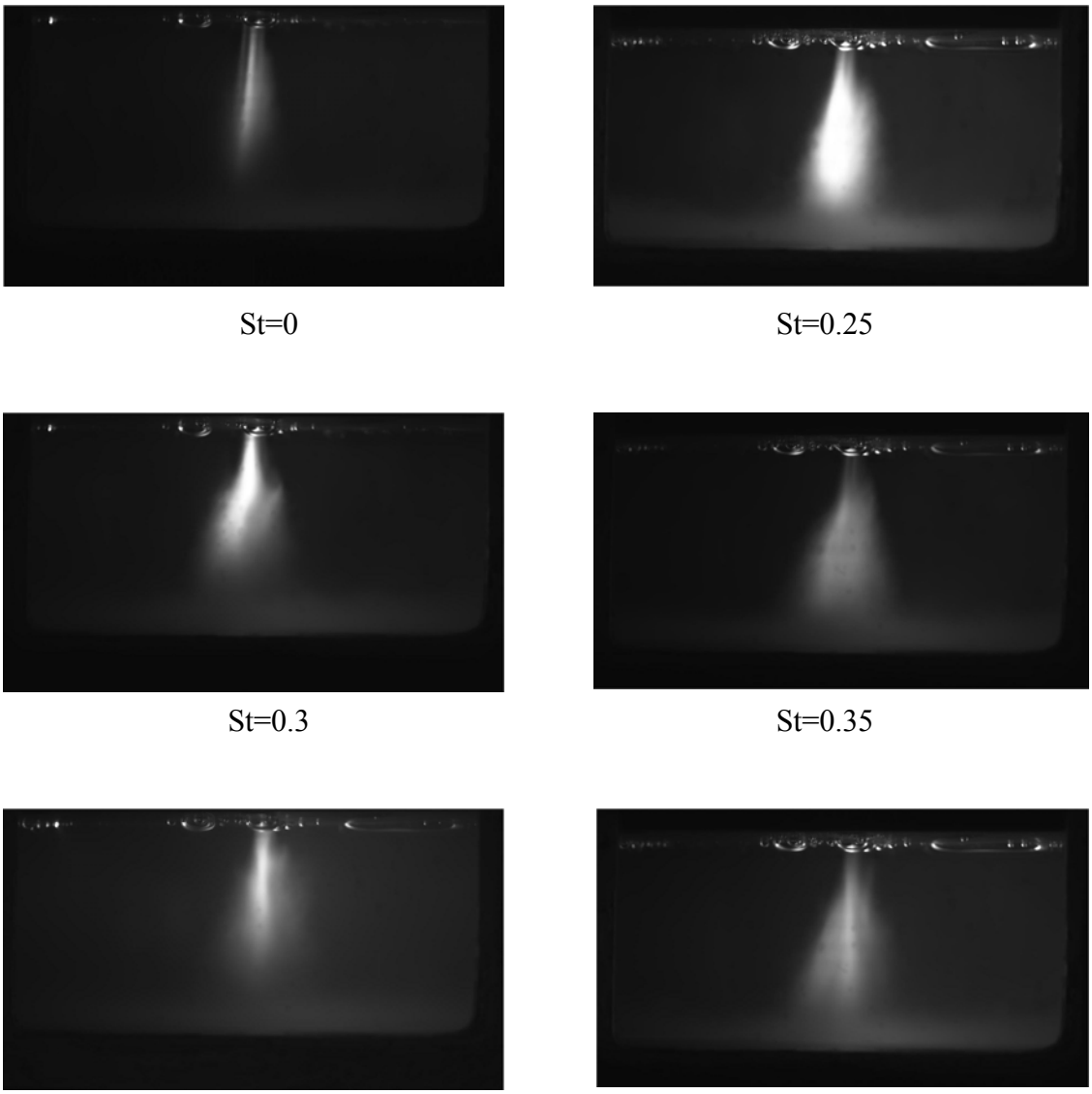

Figure 5.16. Average images at different Strouhal numbers for Re=10000, Z/D=6

(cont. on next page)

St=0.6

St=0.65

St=0.75

St=0.85

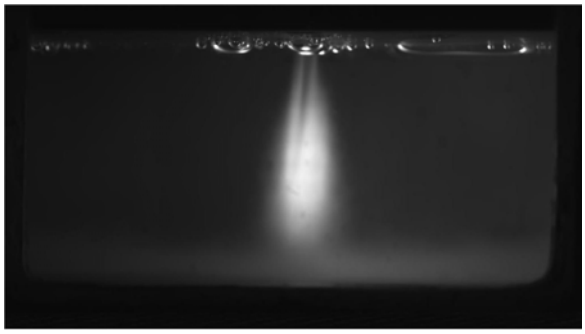

St=1

Figure 5.16. (Cont.)

For velocity and turbulence intensity measurements are once performed for non-perturbation jets for reference purposes. In these experiments, data are measured at four different cross-sections in z-normal plane. Strouhal number is kept a constant value of 0.5 except for the non-perturbed case in which it is St=0. Mean velocity profiles and turbulence intensity for these experiments are shown in Figure 5.17 and Figure 5.18, respectively. Disorders in the mean velocity data are due to inadequate calibration for low velocities so low velocity occurs far away from the jet axis could not be measured correctly and relatively high turbulence at the inlet. Nevertheless, except for the near flat plate (z/D=5.4) position, rest of the profiles are in close proximity with each other indicating a very small increase in the jet width. This is an expected result for the profiles taken in the close proximity of the nozzle. Moreover, it is seen that jet spreads out near the plate due to the imposed pressure gradient.

Similarly for the turbulence intensity shown in Figure 5.18, there is no change observed among different z/D locations except for the z/D=5.4 where turbulence levels increase dramatically. There is no significant spreading and/or increase for the other profiles because first they are not far away enough from the jet nozzle and secondly still inside of the jet core; therefore, show laminar characteristics.

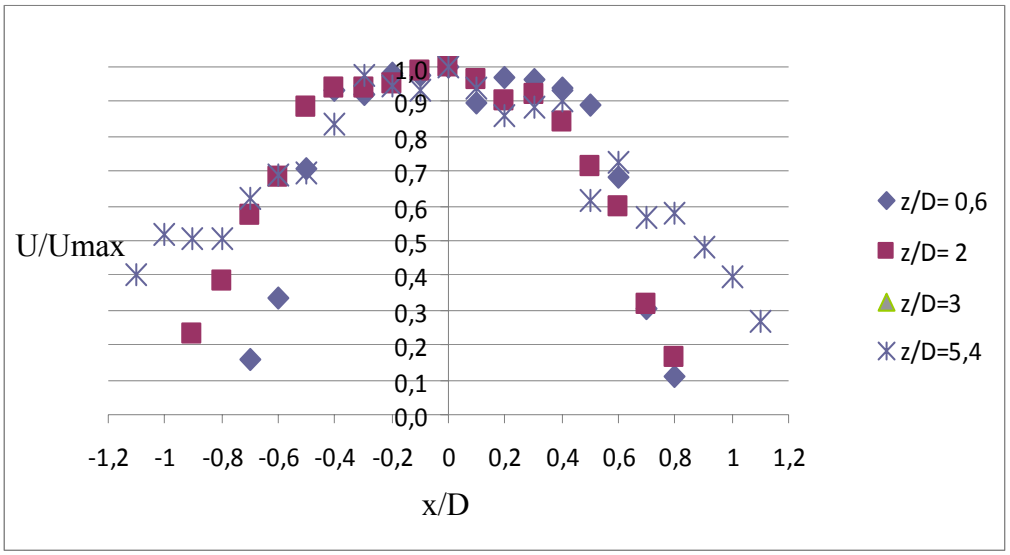

Figure 5.17. Jet velocity profiles at different z plane for non-perturbation jet Re=10000

Increase in the turbulence intensity from the core of the jet towards the outer regions is seen clearly in Figure 5.18. It was expected that there should be some decrease in the intensity when x/D is high enough but due to the shortness of our

traversing mechanism those regions could not be reached and therefore no data are available.

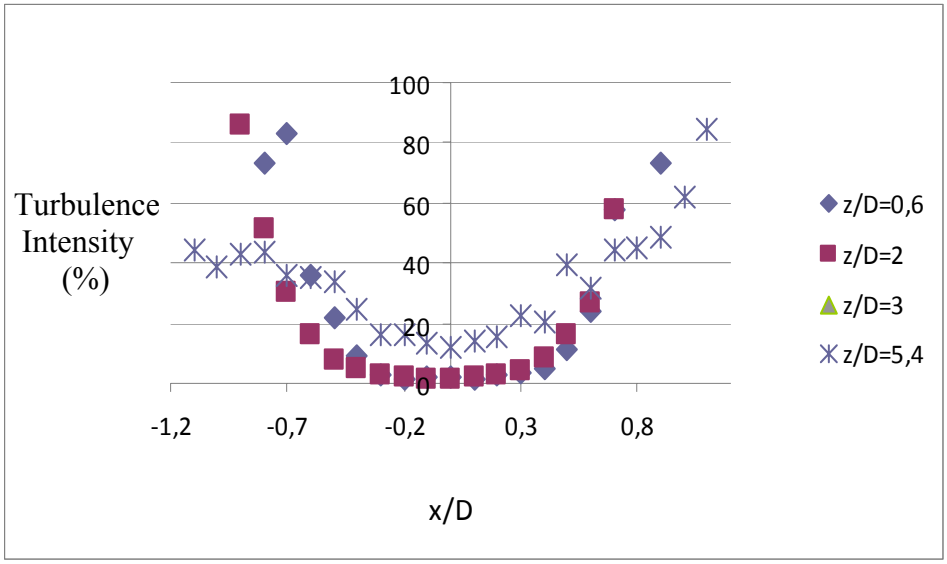

Figure 5.18. Turbulence intensity profile at different z plane for non-perturbation jet Re=10000

Velocity profiles at z/D=0.6 for perturbation of different amplitudes are shown in Figure 5.19. It is easy to see that any increments of the amplitude directly affects the jet flow and increase the jet width at z/D=0.6. However there is no significant difference among effects of the varied amplitudes.

Perturbation amplitude, on the other hand, has no or very slight effect on the mean velocity profiles just at the nozzle exit. This is depicted at Figure 5.19 where z/D is just 0.6. Except for the unperturbed case, all the other profiles corresponding to different amplitudes widen in x normal direction and collapse on each other indicating that even the smallest amplitude has same effect as the largest one at least for this z/D location. Widening indicates slight increase in the shear layer.

The turbulence intensity at the same value of z/D as shown in Figure 5.20, similarly to the mean velocity, there is no any effect into the jet core but due to the increase of the jet width, higher turbulence intensities are now seen in larger x/D locations. The increase of the jet width at this near field of the jet nozzle (small z value) is small but also remarkable since instable modes of the jet has very short time to grow up to this location. Similarly to the mean velocity profiles variations of the amplitudes do not play an important role on the jet width at this plane as well.

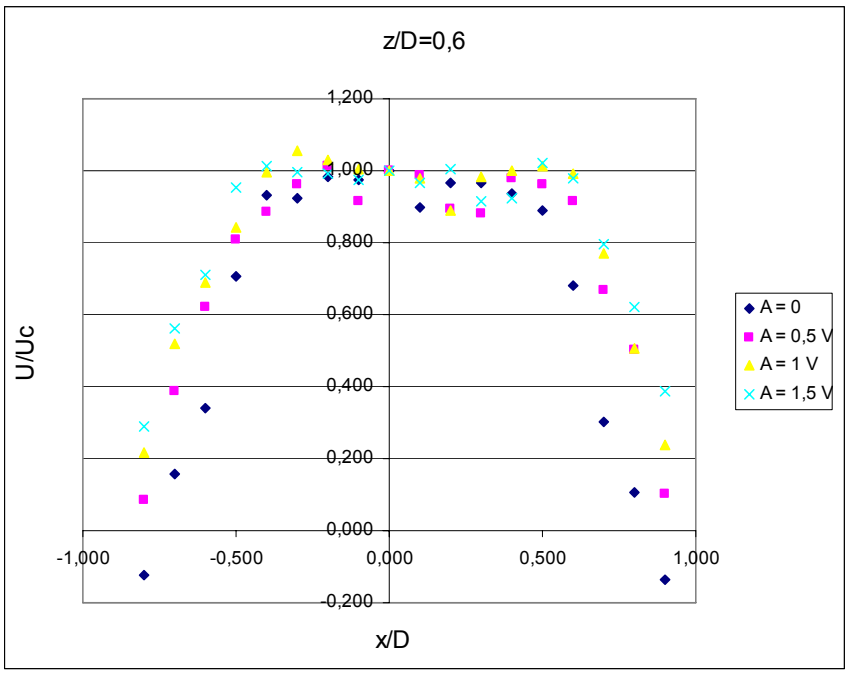

Figure 5.19. Normalized velocity profiles at z/D=0.6 for perturbation of different amplitudes

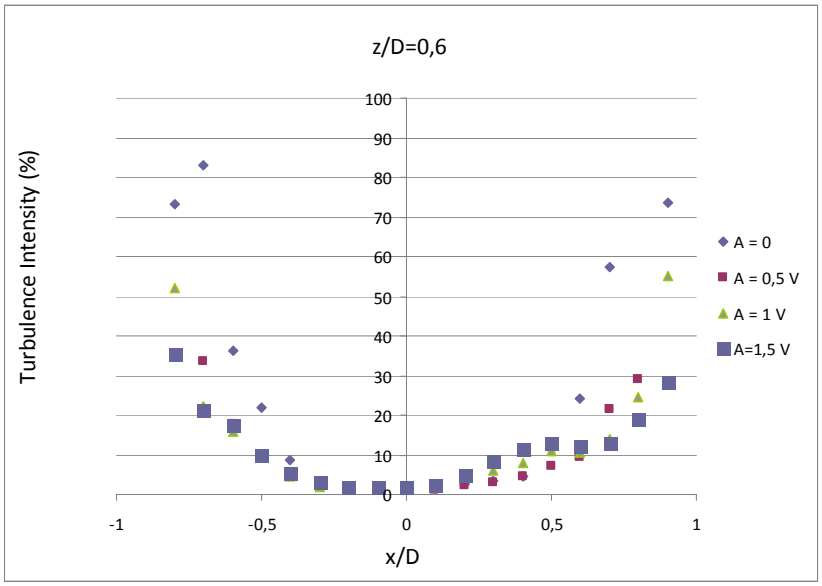

Figure 5.20. Turbulence intensity profiles at z/D=0.6 for perturbation of different amplitudes

The velocity profiles at z/D=2 for different perturbation amplitudes are shown in Figure 5.21. Although the distribution of the data is wide spread, it may be speculated that there might be slight spreading of the velocity profile at the highest amplitude value, A=1.5 V. On the other hand, the turbulent intensities at z/D=2, as shown in Figure 5.22, indicates a decrease in turbulent intensity at the edges of the jet, near the

region of 0.5<x/D<1 and -0.5<x/D<-1. It must be kept in mind that hot-wire data near the edges of the jet has higher error margins due to the very low velocities.

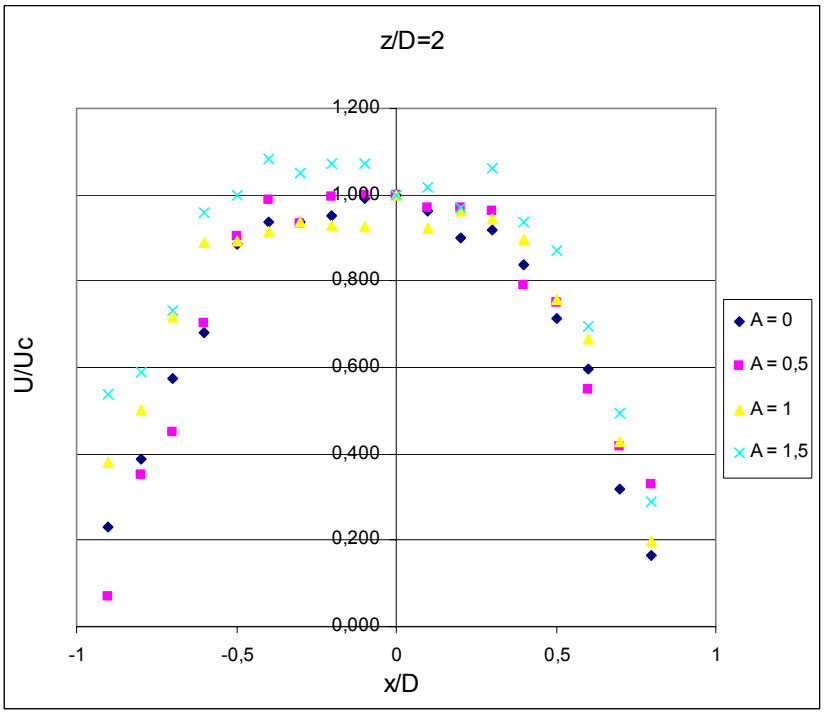

Figure 5.21. Velocity profiles at z/D=2 for different amplitudes.

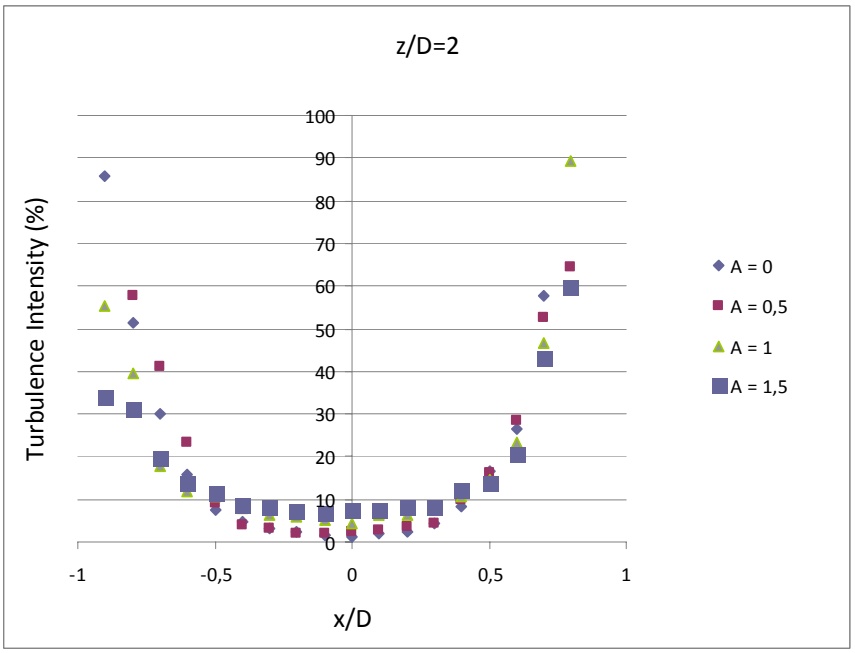

Figure 5.22. Turbulence intensity profiles at z/D=2 for different amplitudes.

Further away from the nozzle at z/D=3, velocity profiles now look smoother and the only effect of the amplitude is at the highest two of them, A=1 and 1.5. However, there is a more striking feature to be observed at the mean velocity profiles which is that the symmetry of the profiles are seemed to be broken for the two largest perturbation amplitudes. This might be due to the unsymmetrical features of the water delivery system in which the sound waves travel before reaching the test section. The spread of the jet with the increasing perturbation amplitudes can be observed but it is very miniscule for the smaller amplitudes and only becomes respectable for the two largest ones. Moreover, note that the jet core region finishes almost at this z distance; this could be observed from the fact that velocity profiles have no straight region in the middle.

The comparison of the velocity profiles at z/D=3 normalized by jet width (b_u) is shown in Figure 5.23. The first striking difference is that our data has a larger $\partial U/\partial x$ and the second one; it is not as wide as the comparison data. These differences might be arising from the fact that in our measurements x and z component velocities could not be separated and therefore our data shows not only x-component of the velocity but a magnitude of x and z components. Another and more probable reason is the differences in the boundaries of our test set up and the comparison. In our setup, outlets are placed comparatively closer to the stagnation center and this condition creates tight circulation regions which might be suppressing the jet spreading than usual.

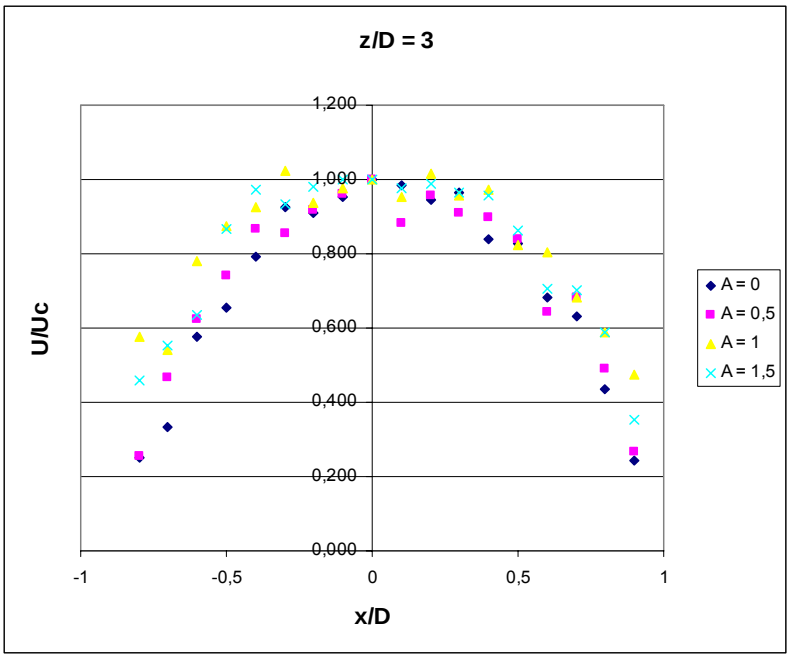

(a)

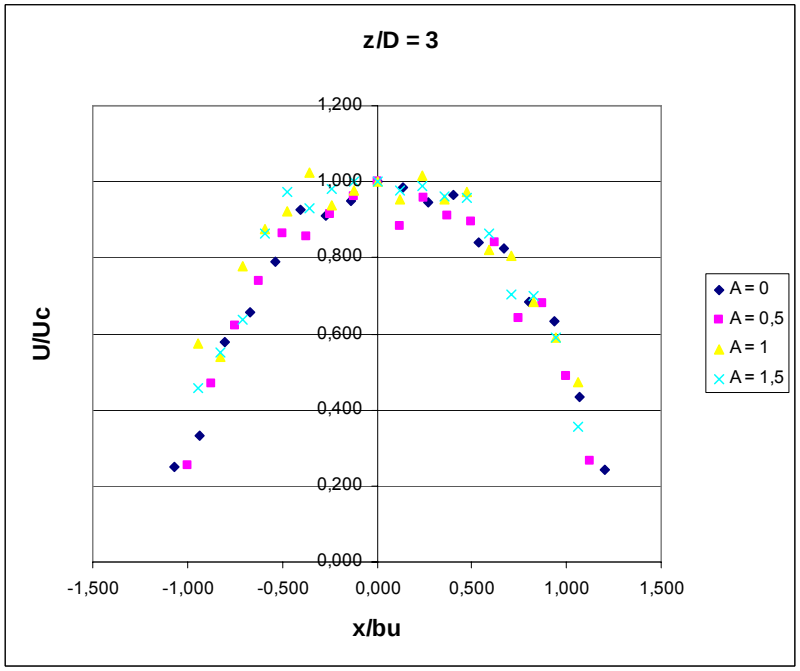

(b)

Figure 5.23. Normalized velocity profile for different amplitudes by jet diameter (a) and jet width (b) at z/D=3.

It is expected that the flow characteristic of the jet shear layer should be turbulent at this z-plane as it was observed at the flow visualizations and this is obviously observed from the higher turbulence intensities. However, there is no

observable effect of various amplitudes on the turbulence intensity as seen in Figure 5.24. The reason is thought to be the longer distance from the nozzle in which the effect of the perturbation is buried in the naturally occurring turbulence.

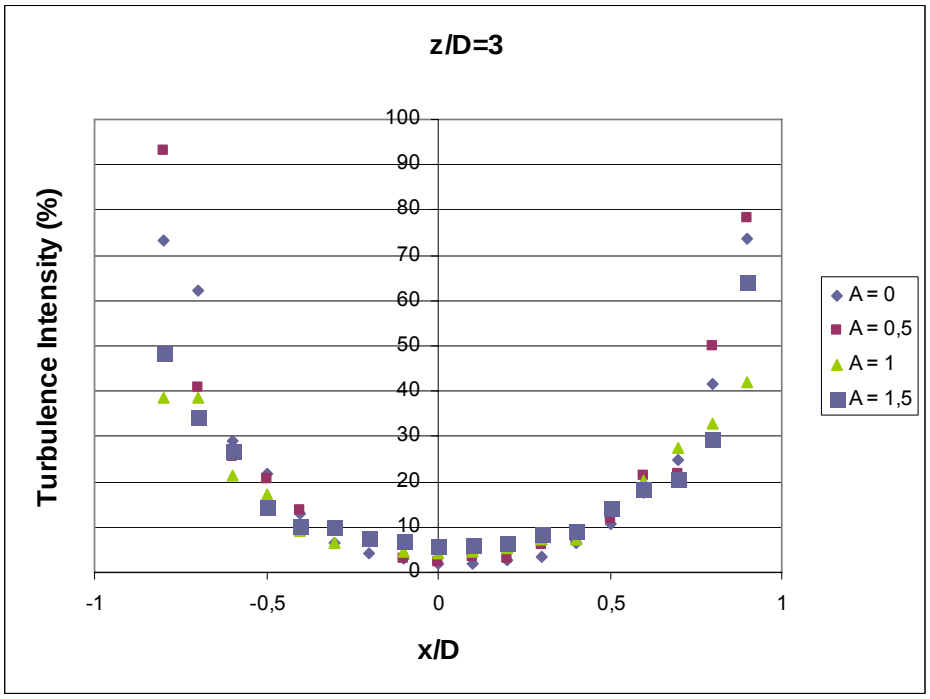

Figure 5.24. Turbulence intensity profile for different amplitudes at z/D=3

We have tried obtaining the jet width trend along the z-axis. The jet width is described as the distance where the velocity is the half of center velocity between either sides of the z-axis. The normalized jet width and its trend line through the jet axis is given in Figure 5.25. Jet width does not change significantly for all amplitudes up to z/D=2. It is thought to be the undesirable disorder of the data needs to be further attention. An increase in the jet width is observed for locations for z/D>2. As a general trend, it can be said that the jet width increases as the perturbation amplitudes increases.

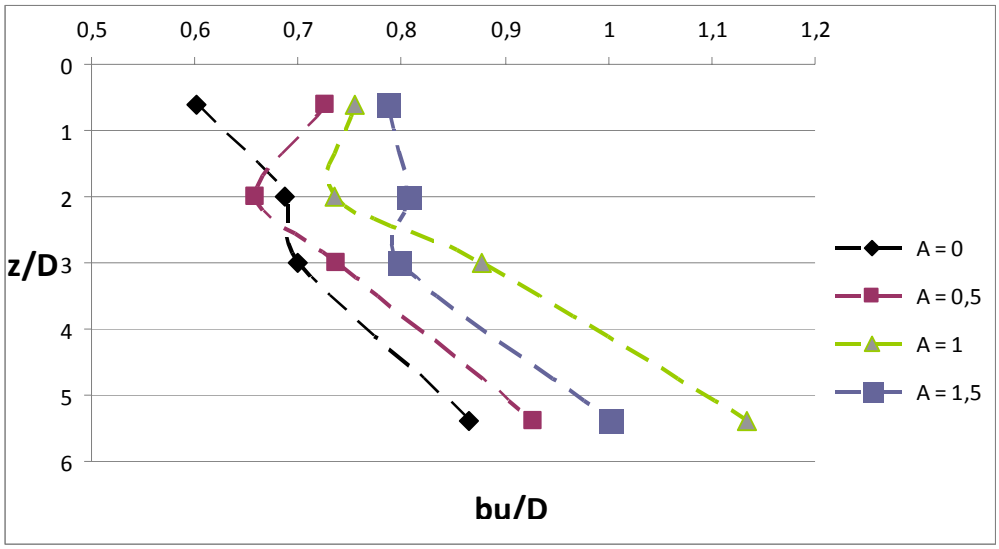

Figure 5.25. Normalized jet width for different amplitudes at St=0.5

5.2.3. Heat Transfer Analysis for Water Jet

Heat transfer measurements of an excited and normal circular round jet are performed for different excitation amplitudes (A) and Strouhal numbers (St) by using a loudspeaker. Figure 5.26 shows local heat transfer distribution at four x/D values[2]. It is easily said that the acoustic excitation decreases the local heat transfer of the jet at the stagnation region. It is an expected situation because excitation increases turbulence intensity in the jet flow and causes an increase in the jet width as seen from the flow visualization experiments given in Figures 5.15 and 5.16. In parallel with this idea, the minimum local heat transfer occurs at St=0.5 where the maximum jet width appears on flow visualization.

[2] Note that all these points are located in the stagnation region; this analysis does not include heat transfer characteristics of wall jet region.

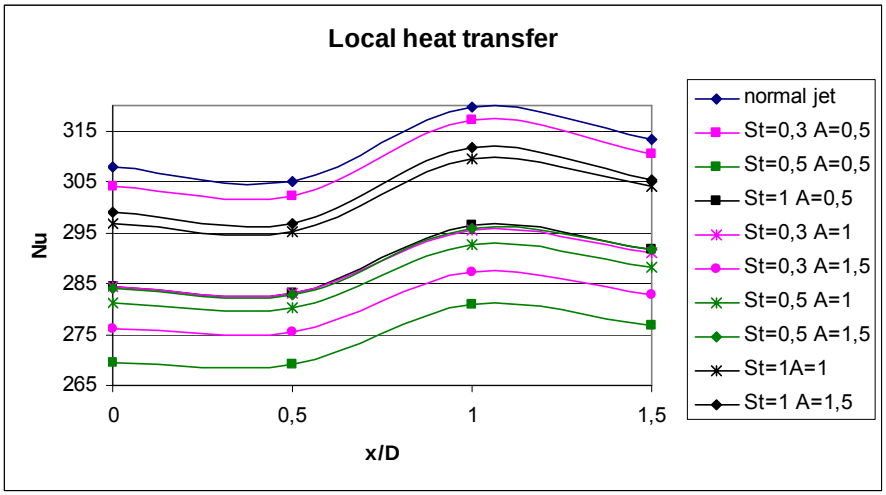

Figure 5.26. Local heat transfer of the jet impingement. Note that "A" in the legend is the voltage send to the loudspeaker amplifier; therefore, it stands for the excitation amplitude.

Average heat transfer coefficient (Nu_{avg}) for different amplitudes is shown in Figure 5.27. This graph shows that the flow at St=0.3 is the most sensitive to the amplitudes among the other Strouhal numbers. The change in the Nusselt number between amplitudes of 0.5 and 1.5 at St=0.3 is nearly two times higher than the others. Interestingly, heat transfer coefficient shows a decreasing trend for St=0.3 as the amplitude increases; however, this trend is reversed at other Strouhal numbers.

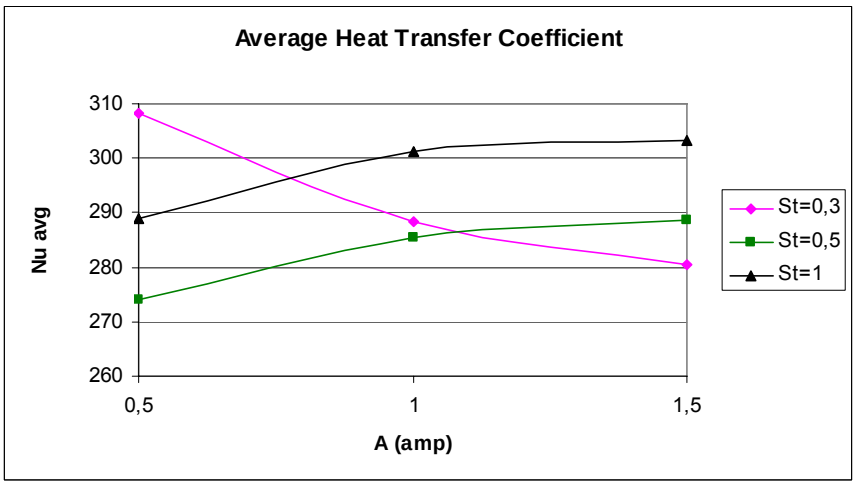

Figure 5.27. Average heat transfer for different amplitudes. Note that the average Nu number for the non-excited jet is near 311.

Effects of Strouhal number on average Nusselt number is shown in Figure 5.28. It is seen that average Nu number is increasing with increasing Strouhal number for St>0.5 region. There is no trend can be seen for the St<0.5 region.

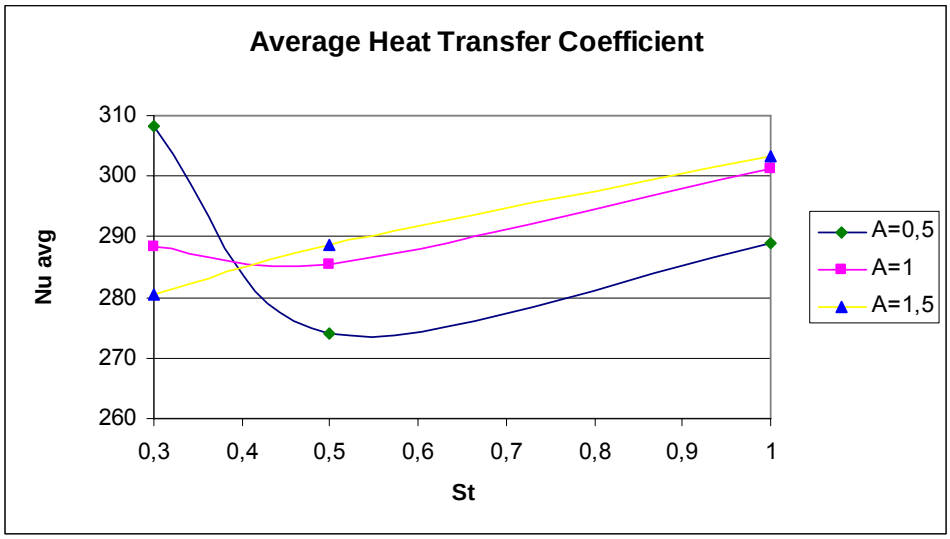

Figure 5.28. Average heat transfer for different Strouhal numbers. Note that the average Nusselt number for the non-excited jet is near 311

CHAPTER 6

CONCLUSION

Heat transfer and flow characteristics of an acoustically excited circular confined jet are experimentally investigated and the results are compared with a non-excited jet. Parameters used on this study are shortly Re=10000, Z/D=6 for dimensionless jet to plate distance, as a non-dimensional excitation frequency Strouhal number is changed in the range of $0<St<1$, and as for the excitation amplitude, voltages sent to the 20X amplifier are 0.5V, 1.0V and 1.5V.

From the numerical results, it has been shown that k-ω turbulence model is recommended rather than the k-ε model for an analysis of jet impingement. Even though predictions of jet velocity profile of these two turbulence models match the experimental data tolerably, their heat transfer predictions of a jet are poor. The magnitude and location of second peak of Nusselt number can not be predicted by them. Its reason was errors of the turbulent kinetic energy solution.

Three kinds of experimental study were performed; flow visualizations, velocity and turbulence intensity measurements by hot-wire anemometer (for water jet) and the last one was heat transfer coefficient measurements by using thermocouples.

From the results of the flow visualization, it has been shown that the jet responses to the acoustic excitation at any level. Jet width increases significantly from z/D=2. Coherent structures in the shear layer and jet width are growing increasingly at $0.25<St<0.55$ whereas they are becoming smaller at $0.55<St<1$. Therefore maximum spreading rate is seen at nearly Strouhal number is equal to 0.5.

According to measurements of velocity and turbulence intensity by hot wire anemometer, we obtained that there is a little difference on the turbulence intensity between normal and excited jets at $0<x/D<0.5$. These little differences might be some importance to the heat transfer characteristics. On the other hand, near the shear layer region, their differences become significant. The excitation decreases the turbulent intensity up to x/D=1, for $x/D>1$ the effect of the jet flow is minimal on the ambient fluid so its turbulence intensity falls down. Velocity distributions of excited and normal jets show parallel trends as the turbulence intensity.

The heat transfer characteristics of excited jets can be summarized that acoustic excitation decreases the local heat transfer of the jet at the stagnation region because the excitation increases turbulence intensity and therefore spreads the jet. Minimum local Nusselt numbers are observed to be occurring at St=0.5 where the maximum jet spread is seen by the visualizations.

The maximum Nu occurs at x/D=1 instead of at the stagnation point (x/D=0). One of the explanations of this situation might be the undesired angle between jet axis and target plate normal thus jet flow could not impinge the target wall perpendicularly.

6.1. Future Works

Some recommendations about the future works for this study may be presented as:

- Nusselt number at wall jet region should be measured. For this, either heated surface area must be increased or the diameter of jet nozzle has to be decreased.
- Alternatively a constant temperature boundary condition can be applied for comparison
- Turbulence structures in the jet flow and how these structures affect Nusselt number should be investigated extensively.
- Flow visualization and hot wire measurements should be done for different Z/D and Reynolds numbers.
- Turbulence intensity and velocity measurements should be performed for wide range of radial distance.
- Effects of initial turbulence intensity should be investigated on the Nusselt number.
- It is recommended that pressure measurements on the impinging plate must be performed
- Extensive velocity measurements ought to be done with optical methods such as Particle Image Velocimetry.
- Different excitation methods can be used in order to compare obtained results with respect to this study, such as fluidic actuators.
- X-wire sensor must be used for velocity and turbulence intensity measurements in order to obtain more than one component of the velocity vector.

REFERENCES

Baughn, J., Shimizu, S. 1991 Heat transfer measurements from a surface with uniform heat flux and an impinging jets. Journal of Heat Transfer, 113, 1023-1025.

Behnia, M., Parneix, S. and Durbin, P.A. 1998 Prediction of heat transfer in an axisymmetric turbulent jet impinging on a flat plate. Int. J. Heat Mass Transfer. Vol 41, No. 12 pp.1845-1855.

Chen, C.-J., Jaw S.-Y. 1998. Fundamentals of Turbulence Modeling, Taylor and Francais, Washington D.C.

Celik, N. and Eren, H. 2009. Heat transfer due to impinging co-axial jets and the jets' fluid flow characteristics, Experimental Thermal and Fluid Science 33, 715-727.

Clifford, A. B. 2005. Acoustics of excited jets-A historical perspective. NASA/TM 2005-213889, Glenn Research Center, Cleveland, Ohio.

Crow, S.C., Champagne, F. H. 1971. Orderly structure in jet turbulence. J. Fluid Mech. 48, 547-591

Den Ouden, C. and Hoogendoorn, C. J. 1974. Local convective heat transfer coefficients for jets impinging on a plate: experiments using a liquid-crystal technique. Proc. 5th Int. Heat Transfer Conf., Tokyo, Japan, September 3-7, 5, 293-297

Gardon, R. and Akfırat, J. C. 1965. The role of turbulence in determining the heat transfer characteristics of impinging jets. Int. J. Heat and Mass Transfer, 8, 1261-1272.

Gardon, R. and Carbonpue, J. 1962. Heat transfer between a flat plate and jets of air impinging on it. Int. Developments in Heat Transfer, Int. Heat Transfer Conf., University of Colorado, CO, USA, August 28 to September 1, 2, 454-460

Gauntner, J. W., Livingood, J. N. B. and Hrycak, P. 1970. Survey of literature on flow characteristics of a single turbulent jet impinging on a flat plate. NASA TN D-5652 NTIS N70-18963

Goldstein, R. J., Behbahani, A. I. and Kieger, H. K. 1986. Streanwise distribution of the recovery factor and the local heat transfer coefficient to an impinging circular air jet. Int. J. Heat Mass Transfer,29, 1227-1235

Hussain, A.K.M.F. and Zaman, M.A.Z. 1981. Turbulence suppression in free shear flows by controlled excitation. J. Fluid Mech. 103, 133-159.

Jambunathan, K., Lai E., Moss, M.A and Button, B.L. 1992 A review of heat transfer data for single circular jet impingement. Int. Journal of Heat and Fluid Flow Vol.13, No13, No 2, June. Department of mechanical Engineering, Nottingham Polytechnic, Nottingham, Uk

Martin, H., 1977. Heat and mass transfer between impinging gas jets and solid surfaces. J. Matter. Process. Technol., 136, 1-3, pp 1-60

Rodi, W.(1975), "A new method of analyzing hot-wire signals in highly turbulent flow and its evaluation in round jets" Disa Information, No. 17.12

Popiel, C. O. and Trass, O.1982. The effect of ordered structure of turbulence on momentum, heat, and mass transfer of impinging round jets. Proc. 7th Int. Heat Transfer Conf., Munchen, Germany, September 6-10, 6, 141-146

Raman,G., Zaman, K.B.M.Q. and Rice, E.J. 1989. Initial turbulence effect on jet evolution with and without tonal excitation. Phys. Fluids A 1(7).1240-1248.

Reichardt, H. 1943. Über ein neue theorie der freien Turbulenz.

Schlichting, H., 1968 Boundary-Layer Theory 6th edition, The McGraw Hill, 696-700

Schlunder, E.U. and Gnielinski, V. 1967. Heat and mass transfer between surfaces and impinging jets. Chem. Ing. Tech., 39, 578-584.

Sibulkin, M. 1952. Heat transfer near the forward stagnation point of a body of revolution. J. Aeronautical Sci., August

Tani, I. and Komatsu, Y.1996. Impingement of a round jet on a flat surface. Proc. Of the 11th Int. Con. Of Applied Mechanics, Springer-Verlag, New York, 672-676

Tollmien, W.1931. Fortschritte der Turbulenzforschung. ZAMM. 33, 200-211

Wilcox, D. C., 2002, Turbulence Modeling for CFD, DCW Industries, La Canada, CA.

Wiltse, J. M. and Glezer,A. 1992. Manipulation of free shear flows using piezoelectric actuators. J. Fluid Mech. Vol. 249, pp. 261-285.

Wiltse, J. M. and Glezer,A. 1998. Direct excitation of small-scale motions in free shear flows. Physics of Fluids, Vol 10, Number 8

Wolf D H ; Incropera F P ; Viskanta R. 1993: "Jet Impingement Boiling", Advances in Heat Transfer.

Yan, X., 1993. A preheated-wall transient method using liquid crystals for the measurement of heat transfer on external surfaces and in ducts. Ph.D. thesis, University of California, Davis.

Zuckerman, N. And Lior, N. 2005. Impingement Heat Transfer: Correlations and Numerical Modeling. Journal of Heat Transfer, The University of Pennysylvania, USA, May